Lightweight design with displacement constraints using graded porous microstructures

Matteo Bruggi[a,], Hussein Ismail[a,b], János Lógó[b], Ingrid Paoletti[c]

[a]*Department of Civil and Environmental Engineering, Politecnico di Milano, Italy*
[b]*Department of Structural Mechanics, Budapest University of Technology and Economics, Hungary*
[c]*Department of Architecture Built Environment and Construction Engineering, Politecnico di Milano, Italy*

Abstract

A multi-scale approach of topology optimization is proposed to design lightweight components for given loads and displacement limits. Hexagonal close-packed arrangements of circular/spherical holes allow defining 2D/3D isotropic/transversely isotropic microstructures whose macroscopic elastic properties depend on the radius of the cavities, namely the density of the porous material. An interpolation law is implemented to handle two-material structures with void, distributing both solid and graded material within a certain density range. An Augmented Lagrangian approach is adopted to handle multiple displacement constraints, along with the enforcement of a minimum amount of graded porous microstructure to be used in the optimal design. The proposed method defines: i) boundaries of the component, and, ii) possible internal arrangements of circular/spherical holes with graded radius. Also, when boundaries of a hollow component are prescribed i), the method can be used to equip it with an optimal infill ii). Numerical examples are presented, concerning two- and three- dimensional problems, for different types of loads. Features of the proposed procedure are discussed, as well as peculiar properties of the optimal solutions, with special regard to coated structures. Fabrication of the porous layouts by means of additive manufacturing techniques is outlined.

Keywords: multi-scale topology optimization, isotropic porous microstructures, close-packing of spheres, multi-constrained optimization, coated structures, additive manufacturing.

Email addresses: matteo.bruggi@polimi.it (Matteo Bruggi), hussein.ismail@emk.bme.hu,hussein.ismail@polimi.it (Hussein Ismail), logo.janos@emk.bme.hu (János Lógó), ingrid.poaoletti@polimi.it (Ingrid Paoletti)

1. Introduction

Given a geometric domain, topology optimization allows designing structural components by searching for the distribution of material that minimizes an objective function for a prescribed set of constraints [1]. Among the others, the design operated by distribution of isotropic material is widely adopted by academia and industry to sketch lightweight components. Assuming as unknown the density field that governs the elastic modulus of the material, an optimization problem can be formulated to minimize the work of the external loads at equilibrium (the so-called structural compliance), with constraints on the allowed amount of material (the available volume fraction), see [2]. A strong penalization of the intermediate densities was especially conceived in the Solid Isotropic Material with Penalization (SIMP) [3] to achieve optimal layouts made of void ("0" or "white") and solid material ("1" or "black"). The solutions for minimum compliance (i.e. minimum overall strain energy) usually consist of statically determinate truss-like structures that leverage the axial stiffness of struts and ties to get minimum deformability out of a limited amount of material.

Additive manufacturing (AM) is well-suited to bring layouts from concept to reality. It remarkably reduces limitations due to conventional manufacturing techniques, and is nowadays emerging as a competitive alternative to subtractive manufacturing in many fields of application. Indeed, 3D-printing allows for customizable products that can be effectively tailored to meet performance needs and requirements exploiting topology optimization. Reference is made to [4–6] for reviews on recent trends and achievements in their combined use.

Lattice structures are an example of complex features that can be easily manufactured through 3D-printing processes. They can be used to fabricate lightweight, robust and multi-functional infills that are generally preferred over solid interiors for parts of given shape, due to their intrinsic features, see e.g. [7]. Selective Laser Sintering (SLS) can take full advantage of porous infills of any given shape, whereas Fused Deposition Modelling (FDM) requires layouts with a limited overhang, unless printing supports are allowed, see e.g. [8, 9]. In the latter case, a plastic filament is melt and deposed layer-by-layer. For angles exceeding 45° degrees, supports are usually required, since the previous layers are not sufficient to build upon safely.

Optimal infill and external shape can be designed within the same numerical procedure by means of topology optimization. Among the available techniques to solve this design problem, multi-scale topology optimization represents an effective and efficient alternative, see the recent review in [10]. Assuming a separation of scales, numerical homogenization can be conveniently adopted to model the periodic microstructure of the infill (micro- or meso- level) by using equivalent material properties at the macro-scale, see e.g. [11–13]. Asymptotic homogenization can be employed to compute the effective elastic properties of lattice material in terms of one or more design variables, i.e. one or more geometrical parameters governing a microstructure to be graded within the design domain, see e.g. [14, 15]. Alternatively, a procedure of inverse homogenization is needed to derive the shape of the microstructure corresponding to intermediate values of the unknown density field, see e.g. [16, 17]. It must be remarked that inverse homogenization was exploited in the early stages of topology optimization to circumvent the ill-posedness of the continuous problem that distributes a "void" and a solid phase only. Composites were allowed to occur at intermediate densities to this goal, see in particular [18] and [19].

In both cases, the achieved microstructures may be difficult to fabricate. When several patterns are generated, see e.g. [20], a peculiar issue is that different patches cannot be easily merged altogether. Loss of continuity or undesired geometrical singularities are likely to arise, unless this has been explicitly taken into account in the formulation, see e.g. [21]. Effective de-homogenization techniques have been proposed in the literature to overcome these problems, see in particular [22] and [23]. When grading honeycombs, see e.g. [24], or lattice and surface-based representations with given topology, see e.g. [25], issues to be faced include handling of anisotropy (especially in 3D), potential weakness of the microstructure (due to any abrupt change in section and sharp connections), features exhibiting critical overhang angles.

Most of the contributions dealing with multi-scale design for maximum stiffness are based on the volume-constrained minimum compliance problem already mentioned. When there is only one loaded point, the work of the external load is given by the scalar product of the displacement along the direction of the applied force and the force itself. Indeed, the same solution (up to a scaling) is expected to arise when considering either a volume-constrained minimum compliance problem or a displacement-constrained minimum volume problem, see [26]. A classical extension of the minimum compliance problem to multiple load cases consists in using a weighted sum of the energy contribution pertaining to each one of the considered load cases. However, when local control of the deflection is requested under the effect of distributed loads, multiple forces and multiple load cases, the enforcement of a set of displacement constraints is required.

Within the above framework, this contribution presents a multi-scale approach of topology optimization to design lightweight components for given loads and prescribed displacement limits. Hexagonal close-packed arrangements [27] of circular/spherical holes allow defining 2D/3D isotropic/transversely isotropic microstructures whose homogenized elastic properties can be graded by varying the radius of the cavities. Due to the moderate anisotropy of the three-dimensional porous material, the macroscopic elastic properties of both porous phases can be derived in terms of the bulk modulus and the shear one. A multi-material interpolation law is introduced to distribute full material, and a graded porous phase with densities belonging to a prescribed range. A void phase is allowed, unless a minimum infill density is prescribed all over the design domain. In addition to the set of local constraints that control the deflection, an enforcement governing the minimum amount of graded porous microstructure in the optimal layout is implemented. Following recent contributions in the area of topology optimization with local stress enforcements, see [28, 29], the arising multi-constrained formulation is tackled by combining sequential convex programming [30] and an Augmented Lagrangian (AL) approach [31]. A simple technique is proposed to post-process the optimal density field to i) extract the boundaries of the component, if any, and ii) provide the internal arrangement of circular/spherical holes with graded radius, intrinsically preserving the material continuity between adjacent cells while avoiding the arising of weak directions. The geometry of two-dimensional and three-dimensional blueprints can be straightforwardly exported for production through additive manufacturing.

The paper is organized as follows. Section 2 focuses on both the two-dimensional and the three-dimensional porous microstructures herein considered. It presents the outcome of the homogenization procedures and introduces the interpolation law adopted to distribute solid and graded material, with void. The multi-scale formulation of topology optimization with displacement constraints is introduced in Section 3, along with details on its numerical implementation and the post-processing approach to get blueprints. Numerical simulations are presented in Section 4, considering several types of load conditions. Peculiar features of the achieved optimal layouts are discussed, as well as their structural performance. Finally, Section 5 draws conclusions and introduces topics of the ongoing research.

2. Material model

2.1. Solid Isotropic Material with Penalization

Given a Cartesian reference frame $Oz_1z_2z_3$, a three-dimensional body made of linear elastic isotropic material with Young's modulus E_0 and Poisson's ratio ν_0 occupies the region Ω. Denoting by σ_{ij} and ε_{ij} the components of the stress tensor and of the strain tensor, respectively, the constitutive relation reads:

$$\sigma_{ij} = (K_0 - 2G_0/3)\varepsilon_{kk}\delta_{ij} + 2G_0\varepsilon_{ij}, \tag{1}$$

where

$$K_0 = \frac{E_0}{3(1-2\nu_0)}, \;\; G_0 = \frac{E_0}{2(1+\nu_0)} \tag{2}$$

are the three-dimensional bulk modulus and the shear modulus of the material, respectively.

Assuming plane stress elasticity, the stress-strain relation becomes:

$$\sigma_{ij} = (K_0 - G_0)\varepsilon_{kk}\delta_{ij} + 2G_0\varepsilon_{ij}, \tag{3}$$

where

$$K_0 = \frac{E_0}{2(1-\nu_0)} \tag{4}$$

is the two-dimensional bulk modulus of the material and G_0 is the shear modulus of Eqn.(2).

In a density-based approach of topology optimization, $0 \leq \rho \leq 1$ is a variable that governs the elastic properties of the material in Ω through the so-called Solid Isotropic Material with Penalization (SIMP) [1, 3]. One may write:

$$K(\rho) = K_{min} + \rho^p(K_0 - K_{min}), \qquad G(\rho) = G_{min} + \rho^p(G_0 - G_{min}), \tag{5}$$

where $p > 1$ (usually $p = 3$) is intended to penalize the intermediate range of the density, K_0 is either the three-dimensional bulk modulus of the material or its plane-stress two-dimensional counterpart, depending on the problem, and G_0 is the shear modulus. K_{min} and G_{min} are small nonzero values to be used when computing the solution of the elastic equilibrium of the body via finite element analyses (typically 10^{-9} times the values at full material). Polylactic acid (PLA) is assumed in this study as the reference material, being $E_0 = 3.6\,\mathrm{GPa}$ and $\nu_0 = 1/3$.

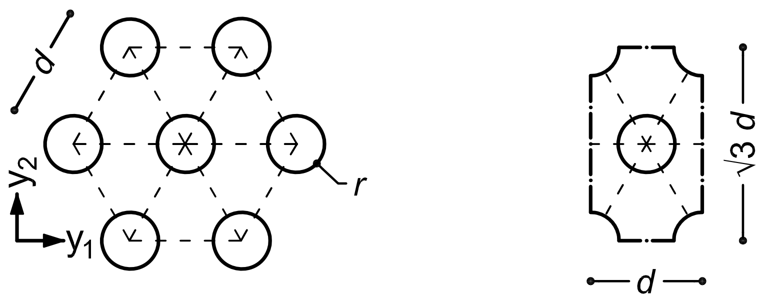

(a) (b)

Figure 1: 2D version of the porous microstructure: hexagonal arrangement of circular holes, with prescribed reference dimension d and variable radius r (a); a single base cell (b).

2.2. A porous microstructure with graded circular holes

As investigated e.g. in [32], an hexagonal arrangement of circular holes gives rise to a 2D isotropic porous microstructure, see Figure 1. This geometry is quite similar to that of the extreme periodic microstructure found in [33] when using inverse homogenization to maximize the bulk modulus with isotropy constraint, see also [34]. Similarities arise also with respect to some of the base cells presented in [35], where the design for optimized strength against initiation of microscopic buckling is dealt with considering different load cases. It must be also remarked that rounded holes are effective in preventing the arising of undesired stress concentration, see in particular the numerical investigations on material design reported in [36] and [37].

The material density of a two-dimensional graded porous microstructure featuring an hexagonal arrangement of circular holes can be computed as $\rho_g = 1 - |Y_v|/|Y|$, where $|Y|$ is the volume of the base cell with dimensions $l_{y1} = d, l_{y2} = \sqrt{3}d$ and $|Y_v|$ is the volume of the inner circular-like

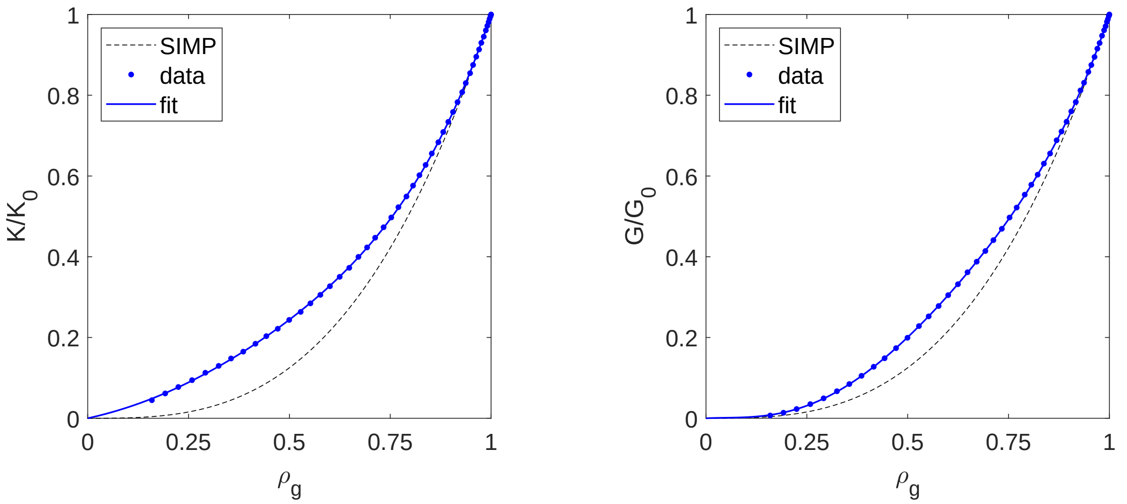

(a) (b)

Figure 2: 2D version of the porous microstructure: interpolation laws fitting results from numerical homogenization, as compared to the conventional SIMP: two-dimensional bulk modulus $K(\rho_g)/K_0$ (a); shear modulus $G(\rho_g)/G_0$ (b).

voids. The density depends upon the radius of the circular holes as:

$$\rho_g = 1 - \frac{2\pi r^2}{\sqrt{3}d^2} \quad \text{for} \quad 0 \leq r \leq r_{max}, \quad \text{with} \quad r_{max} = \frac{d-t}{2}, \tag{6}$$

where r_{max} is the maximum radius as a function of the reference dimension of the microstructure, d, and of the minimum thickness of the material between two adjacent holes, t. For $t = 0$, the density of the material would be that of a close-packing of circular holes, i.e. $\rho_{g,min} = 0.093$, see [27].

The dependence of the stress-strain matrix on the material density may be evaluated by performing numerical homogenization on the base cell represented in Figure 1(b). The pixel-based method implemented in [38] is used. Homogenization is run using a regular mesh with pixel dimen-

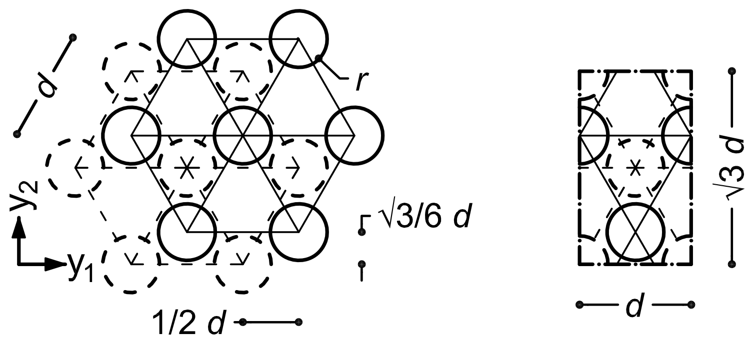

(a) (b)

Figure 3: 3D version of the porous microstructure: superposition of hexagonal layers of spherical holes in the hexagonal close-packed (HCP) arrangement, with prescribed reference dimension d and variable radius r (a); plan view of a single base cell (b).

sion $l_{pix} = d/100$, for $0 \leq r < r_{max}$, assuming $t = d/50$ (the material disintegrates for $t = 0$). The achieved results are fitted using a fifth degree polynomial, for which zero stiffness is additionally enforced at $\rho_g = 0$. The material law reads:

$$\begin{aligned} K(\rho_g) &= K_{min} + \left(1.0483\rho_g^5 - 1.1636\rho_g^4 + 0.3993\rho_g^3 + 0.4950\rho_g^2 + 0.2210\rho_g\right)(K_0 - K_{min}), \\ G(\rho_g) &= G_{min} + \left(3.5149\rho_g^5 - 7.6208\rho_g^4 + 5.7678\rho_g^3 - 0.7083\rho_g^2 + 0.0465\rho_g\right)(G_0 - G_{min}), \end{aligned} \tag{7}$$

for $0 \leq \rho_g \leq 1$, where K_0 and G_0 are the full material values introduced in Section 2.1 for plane stress, namely K_0 of Eqn. (4) and G_0 of Eqn. (2), whereas K_{min} and G_{min} are those of Eqn. (5).

In Figure 2, the fitting interpolation laws are compared to the conventional SIMP to point out that the porous microstructure is much stiffer at low and intermediate densities than the conventional penalization with $p = 3$. This applies especially for the two-dimensional bulk modulus.

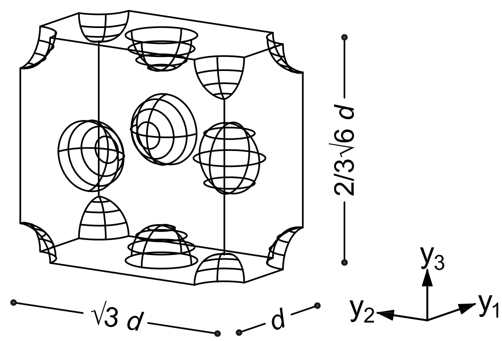

Figure 4: 3D version of the porous microstructure: three dimensional view of a single base cell.

2.3. A porous microstructure with graded spherical holes

In geometry, close-packing of equal spheres is a dense arrangement of congruent spheres in an infinite, regular arrangement [27]. There are two simple periodic layouts that achieve the highest average density, namely the Face-Centered Cubic (FCC), also called Cubic Close-Packed, and the Hexagonal Close-Packed (HCP) .

In Figure 3, a sequence of two hexagonal layers of spherical holes in the so-called hexagonal close-packed arrangement is represented. The layer A has the same arrangement already used for circular holes in the 2D porous microstructure. It is represented using dotted lines. The layer B is found by translating the layer A along a vector $(1/2\ d, \sqrt{3}/6\ d, \sqrt{6}/3\ d)$, as depicted using continuous lines in the picture. A six-fold rotational symmetry about the y_3-axis, perpendicular to the hexagonal layers, is observed in the microstructure. Hence, the periodic sequence AB gives rise to a transversally isotropic porous microstructure with axis y_3. It must be remarked that the HCP arrangement achieves the highest average density in the close-packing of equal spheres, herein spherical holes. The FCC layout shares the same geometrical property, but has no transverse isotropy, see [39].

The material density of the three-dimensional graded porous microstructure depends upon the

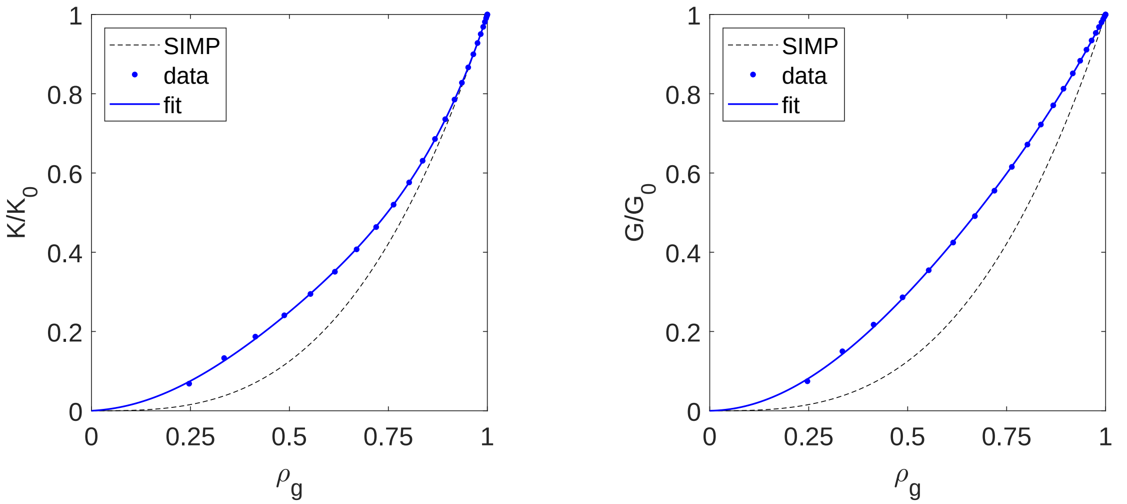

Figure 5: 3D version of the porous microstructure: interpolation laws fitting results from numerical homogenization, as compared to the conventional SIMP: three-dimensional bulk modulus $K(\rho_g)/K_0$ (a); shear modulus $G(\rho_g)/G_0$ (b).

radius of the spherical holes as:

$$\rho_g = 1 - \frac{8\pi r^3}{3\sqrt{2}d^3} \quad \text{for} \quad 0 \leq r \leq r_{max}, \quad \text{with} \quad r_{max} = \frac{d-t}{2}, \tag{8}$$

where r_{max}, d, and t have been already defined in Section 2.2. For $t = 0$, the minimum density of the material would be that of a close packing of spherical holes i.e. $\rho_{g,min} = 0.259$.

For transversally isotropic material the stress-strain relationship is a function of five independent parameters. Its dependence on ρ_g can be evaluated by applying the voxel-based homogenization approach presented in [40] to the base cell of Figure 4. Homogenization is run assuming PLA and a regular mesh with voxel dimension $l_{vox} = d/50$ for $0 \leq r \leq r_{max}$, see Eqn. (8), with the same minimum thickness already used for the 2D base cell. According to Appendix A, the 3D porous microstructure is affected by minor anisotropy. As a simplification, isotropic material modelling will be used in the following.

Along the lines of the procedure followed in the two-dimensional framework, the results achieved through homogenization are fitted using a fifth degree polynomial, for which zero stiffness is additionally enforced at $\rho_g = 0$. The material law reads:

$$\begin{aligned} K(\rho_g) &= K_{min} + \left(1.7267\rho_g^5 - 2.3570\rho_g^4 + 0.6246\rho_g^3 + 0.9517\rho_g^2 + 0.0540\rho_g\right)(K_0 - K_{min}), \\ G(\rho_g) &= G_{min} + \left(0.7420\rho_g^5 - 1.2437\rho_g^4 + 0.2233\rho_g^3 + 1.2634\rho_g^2 + 0.0151\rho_g\right)(G_0 - G_{min}), \end{aligned} \tag{9}$$

for $0 \leq \rho_g \leq 1$, where K_0 and G_0 are those of Eqn.(2), whereas K_{min} and G_{min} have been introduced in Section 2.1. The fitting interpolation laws $K(\rho_g)$ and $G(\rho_g)$ are represented in Figure 5, along with the conventional SIMP for $p = 3$. The main consideration set out with regard to the two-dimensional results of Figure 2 applies here as well. With respect to SIMP with $p = 3$, the increase in terms of shear modulus is even bigger than that in terms of bulk modulus.

2.4. A two-phase material model with void

A two-phase interpolation law for the isotropic elastic constants is introduced to allow for the distribution of full material and void (see Section 2.1), along with a fraction of porous microstructure with graded circular/spherical holes (see Sections 2.2/2.3). It reads:

$$\begin{aligned} K(\rho, \rho_g) &= \rho^p K_0 + (1 - \rho^p) K(\rho_g), \\ G(\rho, \rho_g) &= \rho^p G_0 + (1 - \rho^p) G(\rho_g), \end{aligned} \tag{10}$$

for $0 \leq \rho, \rho_g \leq 1$, where symbols are those already used in Eqns. (5), (7) and (9). For $\rho = 1$, whatever the value of ρ_g, the bulk modulus and the shear one are those of full material, i.e. K_0 and G_0 respectively. For $\rho = \rho_g = 0$, only the terms K_{min} and G_{min} are nonzero, i.e. the fictitious stiffness of the void is found, see Eqns. (7) and (9). For $\rho = 0$ and $\rho_g \neq 0$ a porous microstructure may arise according to the adopted interpolation, either Eqn. (7) or Eqn. (9).

In the above equations, the penalization of ρ is especially conceived to steer the design towards its limit values, i.e. $\rho = 1$ (full material) or $\rho = 0$ (void or porous microstructure graded by ρ_g). Indeed, increasing ρ on a certain place automatically reduces the weight of the complementary phase, thus promoting 0-1 design. Formulations to distribute two distinct materials and void (three phases) using this concept were introduced in [41], as reviewed by [42].

To enhance the effect of such an approach, p is smoothly increased during the simulations from 3 to 6 through a continuation approach, see [43].

3. Design for minimum weight under displacement constraints

3.1. Formulation

A finite element discretization of a given design domain is operated, using four-node and eight-node displacement-based elements in two and three dimensions, respectively. Two sets of element-wise design variables are considered to implement the material law of Eqn. (10). In the e-th of the n elements of the mesh, ρ_e and $\rho_{g,e}$ are the discrete counterpart of the variables ρ and ρ_g, respectively.

A problem for the design of a topology of minimum weight under displacement constraints can be stated as:

$$\begin{cases} \displaystyle \min_{\substack{0 \le \rho_e \le 1 \\ 0 \le \rho_{g,e} \le \rho_{g,max}}} W = \sum_{e=1}^{n} \Big(\rho_e + (1-\rho_e)\rho_{g,e} \Big) W_{0,e} & \text{(11a)} \\ \text{s.t.} \;\; \mathbf{K}(\boldsymbol{\rho}, \boldsymbol{\rho_g})\, \mathbf{U}_j = \mathbf{F}_j, \quad \text{for} \;\; j = 1...l, & \text{(11b)} \\ \quad u_i \le u_{lim,i}, \quad \text{for} \;\; i = 1...m, & \text{(11c)} \\ \displaystyle \quad \sum_{e=1}^{n} (1-\rho_e)\rho_{g,e}\, W_{0,e} \ge f_g \sum_{e=1}^{n} W_{0,e}. & \text{(11d)} \end{cases}$$

In the above statement, the objective function is the weight of the component, which is computed through the sum of the element contributions $(\rho_e + (1-\rho_e)\rho_{g,e})\, W_{0,e}$, being $W_{0,e}$ the volume of the e-th element for $\rho_e = 1$.

Eqn. (11b) prescribes the discrete elastic equilibrium. The global stiffness matrix $\mathbf{K}(\boldsymbol{\rho}, \boldsymbol{\rho_g})$ is computed by assembling the element contributions that account for the constitutive law given in Eqn. (10). Each of them may be conveniently written as the sum of a contribution depending on the interpolation of the bulk modulus $K(\rho_e, \rho_{g,e})\mathbf{K}_{K0,e}$, and a contribution depending on the shear modulus $G(\rho_e, \rho_{g,e})\mathbf{K}_{G0,e}$, where $\mathbf{K}_{K0,e}$ and $\mathbf{K}_{G0,e}$ both refer to $\rho_e = 1$, see also [44]. For the j-th of the l load cases, $\mathbf{F}_j$ is the load vector, whereas $\mathbf{U}_j$ is the corresponding nodal displacement vector.

The i-th of the m displacement components to be controlled is denoted by u_i. Eqn. (11c) enforces a prescribed limit $u_{lim,i}$, where $u_{lim,i}$ stands for the relevant maximum displacement allowed. Assuming that u_i is an entry of $\mathbf{U}_j$, i.e. that the i-th displacement constraint refers to the j-th load case, one has:

$$u_i = \mathbf{L}_i^T \mathbf{U}_j, \tag{12}$$

where $\mathbf{L}_i$ is a vector made of zeros except for the entry referring to the i-th displacement degree of freedom, which takes unitary value.

Eqn. (11d) prescribes a minimum value for the weight fraction of the porous microstructure, namely f_g.

As discussed in Section 2.2 and 2.3, a lower bound $\rho_{g,min}$ applies to avoid collapse of the HCP layout of circular/spherical holes. Also, un upper bound $\rho_{g,max}$ should be prescribed to prevent cavities with radii that are too small with respect to the adopted manufacturing technique. The upper bound is enforced in Eqn. (11) through the statement of side constraints for the variables $\rho_{g,e}$. The same technique cannot be used to enforce $\rho_{g,min}$, since, according to Eqn. (10), the void phase arises for $\rho = \rho_g = 0$. To prevent values in the undesired range $0 < \rho_g < \rho_{g,min}$ a projection approach can be conveniently implemented when dealing with the simultaneous design of the boundaries of the component and of the internal graded microstructure. Alternatively, when a problem of optimal infill is considered, both $\rho_{g,min}$ and $\rho_{g,max}$ can be straightforwardly enforced through side constraints.

3.2. Numerical implementation

Details are given in the following sections on the treatment of the density fields to avoid well-known numerical instabilities and achieve a manufacturable porous phase. The gradient-based approach adopted to address the multi-constrained formulation is presented, as well.

3.2.1. Filtering

A standard linear filter [45, 46] is implemented on the element variables ρ_e to avoid potential issues that are well-known in topology optimization, i.e. the arising of mesh dependence and checkerboard patterns. The original variables ρ_e and $\rho_{g,e}$ are mapped to the new sets $\tilde{\rho}_e$ and $\tilde{\rho}_{g,e}$ as follows:

$$\tilde{\rho}_e = \frac{1}{\sum_n H_{es}} \sum_n H_{es}\, \rho_e, \quad \tilde{\rho}_{g,e} = \frac{1}{\sum_n H_{es}} \sum_n H_{es}\, \rho_{g,e} \tag{13a}$$

$$H_{es} = \max(0, r_f - \mathrm{dist}(e,s)), \quad H_{g,es} = \max(0, r_{g,f} - \mathrm{dist}(e,s)) \tag{13b}$$

where $\mathrm{dist}(e,s)$ is the distance between the centroid of the e-th and s-th element, whereas r_f and $r_{g,f}$ are the filter radius used for ρ_e and $\rho_{g,e}$, respectively.

Then, the filtered densities $\tilde{\rho}_e$ are mapped to the set of projected (physical) densities $\widehat{\rho}_e$ in order to achieve 0-1 solutions, i.e. a clear separation between full material and porous material or void. The formulation proposed in [47] is herein adopted:

$$\widehat{\rho}_e = \frac{\tanh(\beta\eta) + \tanh(\beta(\tilde{\rho}_e - \eta))}{\tanh(\beta\eta) + \tanh(\beta(1-\eta)}, \tag{14}$$

with threshold $\eta = [0, 1]$ and sharpness factor $\beta = [1, \infty]$. The Heaviside function projects densities below the threshold to 0 and densities above it to 1, depending on the value of the sharpness factor, see e.g. [48, 49]. In the numerical section $\eta = 0.5$, whereas β is smoothly increased during the simulations from 2 to 16 by means of the continuation approach in [43].

To enforce the lower bound $\rho_{g,min}$ without jeopardizing the arising of the void phase, filtered densities $\tilde{\rho}_{g,e}$ are mapped to a set of projected densities $\widehat{\rho}_{g,e}$, along the line of the approach proposed by [22], see also [14]. One has:

$$\widehat{\rho}_{g,e} = \tilde{\rho}_{g,e} \frac{\tanh(\beta_g \rho_{g,min}) + \tanh(\beta_g(\tilde{\rho}_{g,e} - \rho_{g,min}))}{\tanh(\beta_g \rho_{g,min}) + \tanh(\beta_g(1-\rho_{g,min})}, \tag{15}$$

with threshold $\rho_{g,min}$ and sharpness factor $\beta_g = [1, \infty]$. The Heaviside function scales $\tilde{\rho}_{g,e}$ such that densities below the threshold are projected to 0, whereas densities above remain unchanged. The sharpness factor β_g is smoothly increased during the simulations using the same continuation approach already introduced for β.

When dealing with the design of the optimal infill for a specimen with given external boundaries, no projection is needed on $\widehat{\rho}_{g,e}$, see Section 3.1.

In the numerical simulations that follow it is assumed that $\rho_{g,min} = 0.30$ and $\rho_{g,max} = 0.85$, both in the two-dimensional and three-dimensional case, if not differently specified.

3.2.2. Solving algorithm

The optimization problem in Eqn. (11) is solved via sequential convex programming, adopting the Method of Moving Asymptotes (MMA) [30] as minimizer. The displacement constraints in

Eqn. (11c) and the weight constraint in Eqn. (11d) are handled by means of an Augmented Lagrangian (AL) approach, as implemented in [28] for minimum weight problems with local stress constraints. The AL method allows reducing the computational cost related to the handling of a large number of local enforcements. Indeed, Augmented Lagrangian approaches have proven effective in solving large-scale multi-constrained problems in two and three dimensions, see in particular [29].

It must be remarked that MMA was ideally conceived to handle problems of structural optimization, including formulations accounting for multiple stress and displacement enforcements, see e.g. [50]. Among the successful applications of MMA, the design of compliant mechanisms involves the non-trivial control of displacement components other than those involved in the definition of the work of the external forces at equilibrium, see in particular [51]. Although the simulations presented next address at most a few hundreds of local enforcements, the AL method has been selected to test this method within the framework of the proposed displacement-constrained two-phase formulation. Indeed, future extensions are aimed to include the handling of larger sets of constraints in multi-scale design problems involving both displacement and stress-based enforcements, see e.g. [52]. As already mentioned in Section 1, when the controlled displacement is that involved in the work of a point force, an enforcement regarding the overall strain energy is being formulated. In most of the simulations presented next, the controlled displacements are those of the loaded nodes when considering distributed loads, multiple forces and multiple load cases. A numerical investigation is performed including a constraint to control a displacement component out of the set of those related to the definition of the compliance. However, no test is performed concerning more challenging applications for the design of compliant mechanisms.

Both the constraints in Eqn. (11c) and Eqn. (11d) can be written in the form:

$$h_l/h_{lim,l} \leq 1, \tag{16}$$

where $h_{lim,l}$ is the upper bound of h_l in the l-th enforcement.

At the k-th AL step, an unconstrained problem is considered whose objective function reads:

$$\mathcal{W} + \frac{1}{m+1} \sum_{l=1}^{m+1} \left(a_l^{(k)} q_l + \frac{b^{(k)}}{2} q_l^2 \right), \quad \text{with} \quad q_l = \max \left(\frac{h_l}{h_{lim,l}}, -\frac{a_l^{(k)}}{b^{(k)}} \right), \tag{17}$$

where $a_l^{(k)}$ is the l-th entry of the vector $\mathbf{a}^{(k)}$ of the lagrangian multiplier estimators, and $b^{(k)} > 0$ is a penalty factor. The function in Eqn. (17) is normalized with respect to the number of constraints, namely $m+1$, to avoid the added term prevail over W.

Following [28], MMA is used to cope with the unconstrained minimization of the normalized function in Eqn. (17), which is in turn adopted to update the current values of the lagrangian multiplier estimators and penalty factor for the $(k+1)$-th step. One has:

$$a_l^{(k+1)} = a_l^{(k)} + b^{(k)} q_l \quad \text{and} \quad b^{(k+1)} = \min \left(\alpha b^{(k)}, b_{max} \right), \tag{18}$$

where $\alpha > 1$ is an update parameter and b_{max} an upper bound against numerical issues. In the numerical simulations, the same input parameters given in [28] are used.

The overall process is repeated until convergence is achieved, i.e. the maximum difference in terms of the values of the set of minimization unknowns ρ_e and $\rho_{g,e}$ between two subsequent steps is less than 10^{-3}.

The adjoint method is used to compute sensitivity and run the gradient-based minimizer, see Appendix B.

3.3. Post-processing for manufacturing

A simple procedure is proposed to get blueprints, extracting the boundaries of the component and prescribing location and grading of the porous phase, with minor modifications between 2D and 3D problems. As a result of the minimization procedure, an optimal distribution of the element unknowns ρ_e and $\rho_{g,e}$ is found throughout the design domain. The boundaries of the object (if they are not known a priori) are detected by processing the distribution of the overall material density, namely $\rho_e + (1-\rho_e)\rho_{g,e}$, thus handling together both the solid material region, i.e. ρ_e, and the graded material one, i.e. $(1-\rho_e)\rho_{g,e}$. The threshold $\rho_{g,min}$ is adopted to detect the final shape of the blueprint: according to the introduced projections, all the regions where the overall material density is less then this value should be considered neither infill nor solid phase, i.e. they should be regarded as void. It must be remarked that the use of $\rho_{g,min}$ as a threshold has a negligible effect on the result of the detection procedure when dealing with the boundary between solid and void. This because of the projection in Eqn. (14). The iso-line computed at $\rho_{g,min}$ is used when dealing with the pixel-based density distribution in 2D. The iso-surface computed at the same threshold is used for the voxel-based material densities in 3D. The region inscribed in the detected/assigned boundaries defines a surface in the former case, and a volume in the latter.

Denoting by i_1, i_2 and i_3 three integer indices starting at the origin of a prescribed reference system, the z_1-, z_2- and z_3- coordinates of the centers of the circular/spherical holes in the adopted HCP arrangement (with base cell dimension d) are given by:

$$\left(i_1 + \frac{1}{2}\mathrm{mod}(i_2 + i_3, 2)\right) d, \quad \left(\frac{\sqrt{3}}{2} i_2 + \frac{1}{2\sqrt{3}}\mathrm{mod}(i_3, 2)\right) d, \quad \left(\frac{\sqrt{6}}{3} i_3\right) d, \tag{19}$$

where the operator "mod" returns the remainder after division of two terms. For the generic hole, the average value of the quantity $(1-\rho_e)\rho_{g,e}$ is computed over the elements falling within a neighbourhood of its center with diameter $d/2$, and denoted by $\overline{\rho}_g$. No hole is allowed if any of the surrounding elements falling within the area defined above has $\rho_{g,e} = 0$ or $\rho_e = 1$. In 2D, according to Eqn. (6), the radius of a circular hole reads:

$$r = \left(\frac{(1-\overline{\rho}_g)\sqrt{3}}{2\pi}\right)^{1/2} d. \tag{20}$$

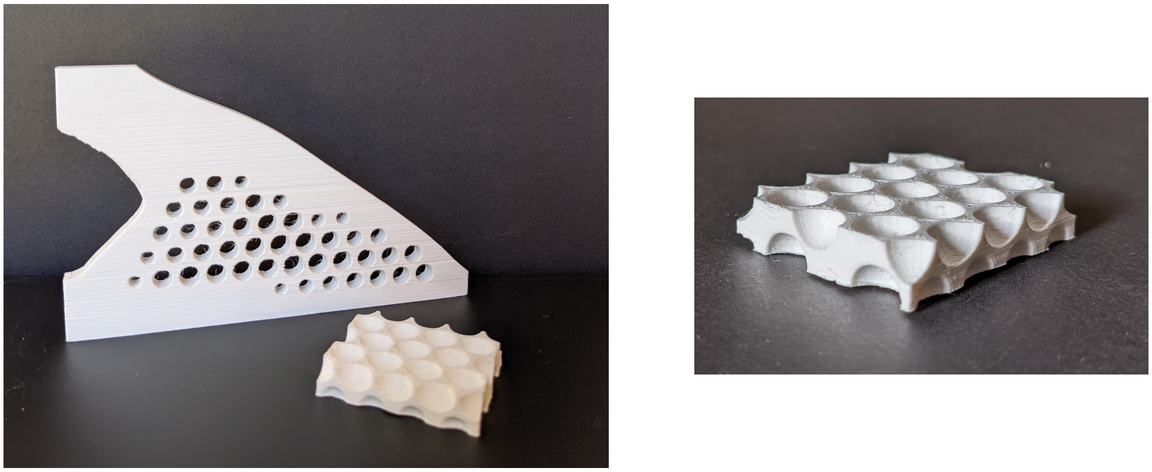

Figure 6: Test specimens fabricated by means of Fused Deposition Modeling.

In 3D, according to Eqn. (8), the radius of a spherical hole reads:

$$r = \left(\frac{(1-\overline{\rho}_g)3\sqrt{2}}{8\pi} \right)^{1/3} d. \tag{21}$$

The final geometry is given by Boolean subtraction of the simple geometrical entities representing the holes (circles or spheres) from the shape representing the region within the external boundaries. The graphical information can be efficiently exported using an Initial Graphics Exchange Specification (IGES) format. Alternatively, a Standard Tassellation Language (STL) format can be used. In the two-dimensional case, a preliminary out-of-plane extrusion is needed to generate a three-dimensional solid. A triangular representation of the involved three-dimensional surfaces (external boundaries of the object along with cylindrical/spherical holes) is performed. A STL writer for the output of voxel-based optimization codes is available e.g. in [53]. Reference is also made to [54] for an insight on CAD-oriented topology optimization.

A few specimens have been manufactured by means of a Fused Deposition Modeling (FDM)

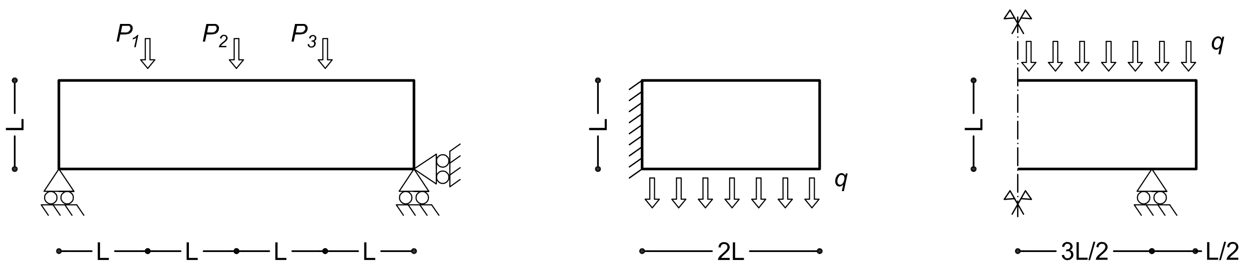

(a) (b) (c)

Figure 7: Geometry and boundary conditions for the two-dimensional numerical examples.

3D-printer to perform a preliminary test with respect to fabrication of the graded porous microstructures herein considered. The samples shown in Figure 6 consist of an optimized cantilever beam with dimensions $125 \times 80 \times 6$ mm and a portion of porous solid material with size $40 \times 20\sqrt{3} \times 10\sqrt{2}/\sqrt{3}$ mm. Samples are as-built, with no finishing. They have been fabricated through deposition of horizontal layers, meaning that the building direction is the vertical one. Cylindrical and (portions of) spherical holes have been all printed with no support. Reference is made in particular to [55] and [56] for discussions on hollowing in FDM and metal 3D-printing, respectively.

It must be remarked that the porous microstructure with graded spherical holes is especially conceived for applications with FDM 3D-printers, i.e. using fused filament fabrication. When dealing with processes employing a bed of fine powders, such as metal-selective laser melting, the unmelted powder has to be removed from any cavity of the printed specimen after fabrication. In this kind of applications spherical holes should be connected by a system of short powder removal channels, in order to employ one of the available strategies to clean the fabricated part [57]. To reduce the invasiveness of the channels, these should preferably be aligned with the direction of maximum stiffness of the porous phase, see Appendix A.

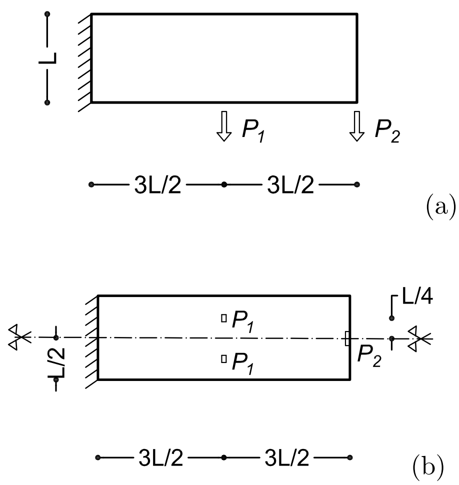

Figure 8: Geometry and boundary conditions for the three-dimensional numerical example: lateral view (a) and view from below (b).

4. Numerical simulations

Numerical examples are presented to assess the method introduced in Section 3, considering two- and three- dimensional applications. The constraints enforced to govern the deflection are such that, in each one of the considered nodes, the controlled component of the displacement cannot overcome α times that computed adopting $\rho = 1$ everywhere (full material in the entire design domain). In the two- dimensional numerical applications of Sections 4.1-4.3 it is assumed that $\alpha = 1.5$, whereas $\alpha = 2.5$ is used for the three-dimensional example of Section 4.4. Geometry and boundary conditions are those presented in Figures 7 and 8. For all the examples, the filter radius r_f used for ρ_e is $L/10$, whereas the filter radius for $\rho_{g,e}$ reads $r_{g,f} = 2r_f$, if not differently specified. Solutions are generated by enforcing different values of $f_g \geq 0$ in the formulation of Eqn. (11). For each numerical investigation, the weight of the achieved optimal design is given in terms of the ratio W/W_0, where W is the weight at convergence and W_0 is the weight of the entire design domain made of full material. All the presented layouts fulfill the enforced displacement

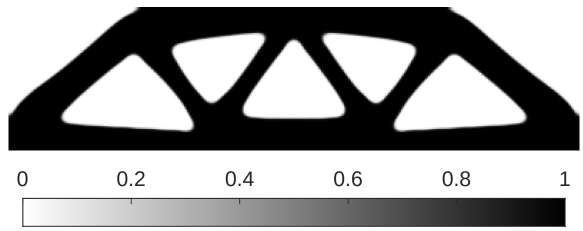

Figure 9: Example 1. Optimal design for $f_g = 0$, $W/W_0 = 0.533$.

constraints.

4.1. Design of a simply-supported beam under multiple load cases

The $4L \times L$ simply-supported beam drawn in Figure 7(a) is addressed, adopting a mesh of 400×100 square finite elements. Four load cases are considered: i) P_1, ii) P_2, iii) P_3, iv) P_1, P_2, P_3 acting simultaneously, with $P_1 = P_2 = P_3$. For each one of the load cases, the displacement control is operated as described above, i.e. enforcing that the vertical displacement at the loaded point/points is not bigger than one and a half times that computed for the full material design domain.

The optimal solution achieved for $f_g = 0$ is shown through the map of element densities $\rho_e + (1 - \rho_e)\rho_{g,e}$ that is represented in Figure 9. A black-and-white statically-determinate truss is found to handle multiple load cases. No phase of grade material is used. The weight at convergence is slightly bigger than half of that of the (full material) reference solution, being $W/W_0 = 0.533$. Indeed, the homogenized material laws derived in Section 2 are such that no advantage arises in terms of stiffness when using intermediate densities instead of full material, see in particular the numerical investigation and experimental tests reported in [10] and [58], respectively.

By adopting $f_g > 0$ in the formulation of Eqn. (11), a minimum amount of graded material is distributed at the cost of an increase in the weight of the optimal solution. This has the

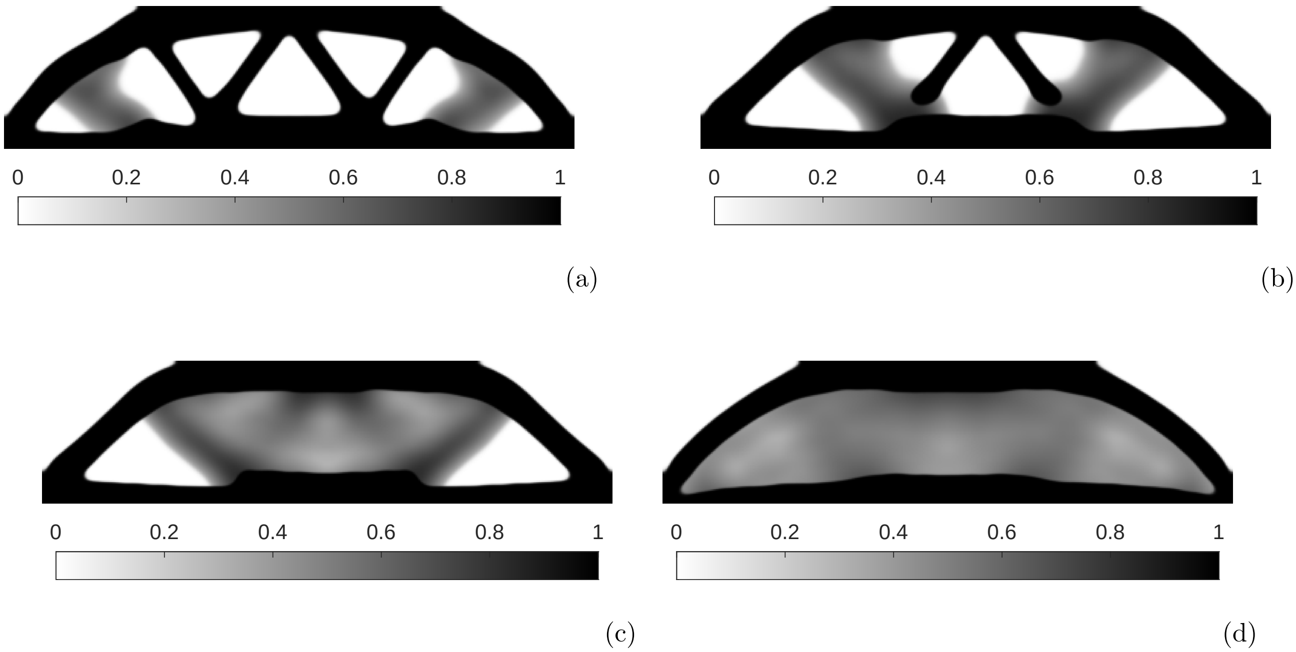

Figure 10: Example 1. Optimal design for: $f_g = 0.05$, $W/W_0 = 0.547$ (a); $f_g = 0.10$, $W/W_0 = 0.555$ (b); $f_g = 0.15$, $W/W_0 = 0.576$ (c); $f_g = 0.20$, $W/W_0 = 0.596$ (d).

aim of exploiting beneficial features that porous microstructures inherently provide, including redundancy of load pathes, high bending stiffness-to-weight ratio, and robustness with respect to force variations, see e.g. [59].

Figure 10 shows the optimal material layouts found by enforcing values of f_g in the range 5-20%, while preserving the structural stiffness of the previous black-and-white solution. All the optimal layouts are characterized by the presence of a solid phase (black), a void phase (white) and a phase of graded material (grey) with density falling in the range $\rho_{g,min}$-$\rho_{g,max}$ (0.30-0.85). For $f_g = 0.05$ some graded material arises to the detriment of the outer inclined members lying below the upper chord in the black-and-white solution. Indeed, the increase in weight is quite low with respect to the solution reported in Figure 9. For $f_g = 0.10$ these members are completely

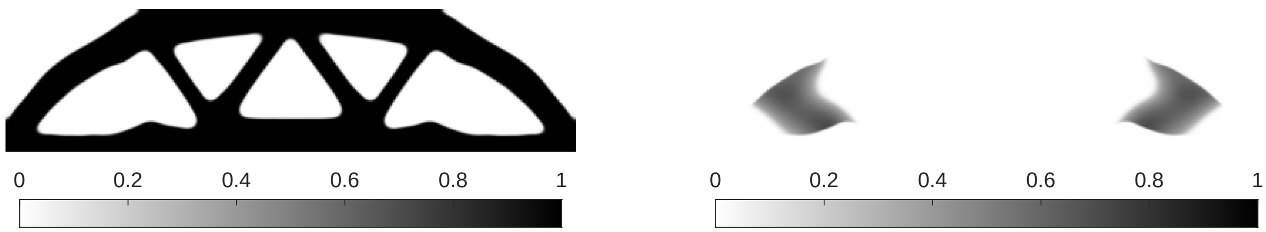

(a) (b)

Figure 11: Example 1. Optimal design for $f_g = 0.05$, $W/W_0 = 0.533$: maps of the distribution of the solid phase ρ_e (a) and of the infill $(1 - \rho_e)\rho_{g,e}$ (b).

replaced by porous material, whereas for $f_g = 0.15$ only the upper and lower chord are made of full material. The latter solution has a weight ratio $W/W_0 = 0.576$, i.e. it is only 8% heavier than the black-and-white solution. The solution found for $f_g = 0.20$ is a variation of that achieved for $f_g = 0.15$, in which the region sandwiched between the upper and the lower solid chord consists of the graded material only. In terms of weight, this coated beam costs around 12% more than the truss design of Figure 10. No void phase arises within the component, meaning that in a layer-by-layer manufacturing process the additional material needed in the printing process is that related to manufacturing of the graded phase only. It must be remarked that specific approaches of topology optimization exist that have been especially conceived to design coated and composite sandwich structures, see in particular [60]-[64]. This kind of structure may spontaneously arise within the proposed procedure, depending on the value of f_g. Differently from the above mentioned contributions, the thickness of the coating, if any, is an outcome of the implemented optimization procedure. However, this could be controlled by leveraging the proposed two-phase material model, that means adopting one of the methods reviewed in [65] to control the minimum and maximum length-scales for the distribution of the minimization unknowns ρ_e. Reference is made also to [66], concerning equal-width length-scale control.

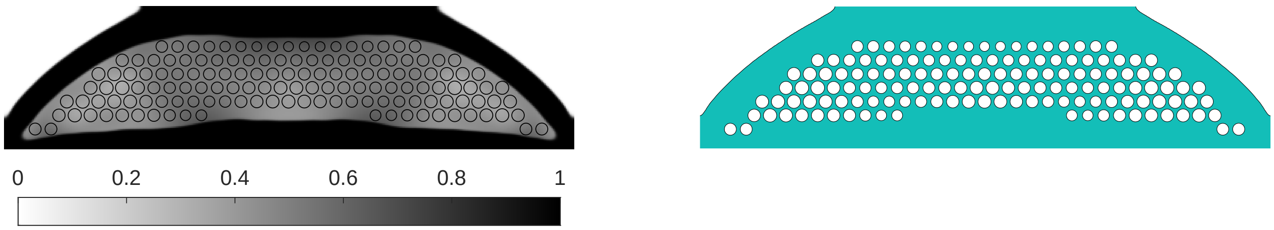

(a) (b)

Figure 12: Example 1. Design for $f_g = 0.20$, d=L/9: overlay of the HPC circular holes and of the optimal distribution of material density (a); final layout (b).

In Figure 11 maps of the distribution of the solid phase ρ_e (a) and of the graded phase $(1-\rho_e)\rho_{g,e}$ (b) are shown separately, concerning the design for $f_g = 0.05$, see Figure 10(a). No overlapping area appears when comparing the two maps of Figure 11, thus assessing the effectiveness of the two-phase material law presented in Section 2.4. Indeed, the adoption of two variables is a key feature to control the amount of graded material in the final layout and to avoid the arising of porous material in the range $\rho_{g,max}$-1. Also, no grey region is found with density value falling below the prescribed lower bound $\rho_{g,min}$.

It has been already remarked that the enforcement of $f_g > 0$ does not generally imply a mere addition of some graded phase to the relevant black-and-white-design. Even in the design achieved for the lowest weight fraction of graded material ($f_g = 0.05$) the solid phase is quite different with respect the solution found when using $f_g = 0$. Indeed, looking at Figure 11(a) in comparison to Figure 9, one may notice not only a different thickness of some elements, but also a particular arrangement of the lower and the upper chord to accommodate the porous phase.

Figure 12 provides a possible final layout for the sandwich component found when optimizing for $f_g = 0.20$, according to the post-processing procedure detailed in Section 3.3. Figure 12(a) shows an overlay of the optimal distribution of material density and of the set of the graded circular

	Load type	Multi-scale design			Full-scale analysis of blueprints		
		Layout	W/W_0	v^{max}	Layout	W/W_0	v^{max}
Ex. 1	$P_1 = P_2 = P_3$	Fig. 9	0.533	7.44	truss	0.555	7.18
		Fig. 10(d)	0.596	7.58	Fig. 12(b) ($d = L/9$)	0.628	6.82
Ex. 2	q	Fig. 14	0.556	4.56	truss	0.569	4.36
		Fig. 15(b)	0.578	4.56	Fig. 17(b) ($d = L/12$)	0.608	4.21
					Fig. 18 ($d = L/16$)	0.598	4.26
	q_{var}				truss	0.569	4.99
					Fig. 17(b) ($d = L/12$)	0.608	4.53
					Fig. 18 ($d = L/16$)	0.598	4.61

Table 1: Multi-scale design vs. full-scale finite element analysis of the blueprints: values of the maximum deflection under the loaded points v^{max} (mm).

holes in a hexagonal-closed-packed arrangement that may be computed for $d = L/9$. In Figure 12(b) the relevant blueprint is depicted.

To improve the match of the grey regions with the distribution of repetitive cells of graded holes (especially in the vicinity of the solid phase), to fully respect separation of length scales, and to minimize any other bias inherent in the post-processing procedure, smaller values of the base cell dimension d may be conveniently used. This mainly depends on the adopted manufacturing technology.

A preliminary numerical investigation is performed to analyze the structural behaviour of the blueprint of the truss represented in Figure 9 and that of the blueprint of the sandwich component shown in Figure 12, by means of full-scale finite element analyses. The final weight ratio for the former layout is $W/W_0 = 0.555$, whereas $W/W_0 = 0.628$ for the latter. Meshes of quadrangular elements have been generated enforcing a maximum edge length equal to $10^{-2}L$, ending up with around $20 \cdot 10^3$ and $25 \cdot 10^3$ elements, respectively. The load case labeled as iv) has been considered, namely P_1, P_2, P_3 (with $P_1 = P_2 = P_3 = P$) acting simultaneously. In both models stiffer regions (square zones with side $L/10$) have been introduced around point forces and restraints, see Figure 7(a), by prescribing a magnified Young's modulus ($\times 10$). These numerical simulations have been

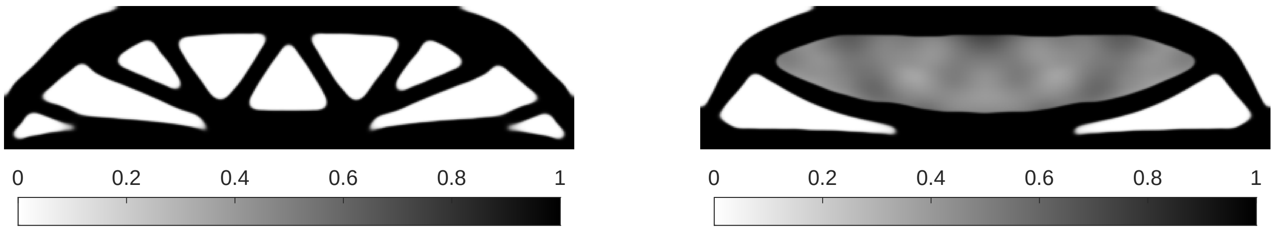

(a) (b)

Figure 13: Example 1. Optimal design, including control on the horizontal displacement at the roller, for: $f_g = 0$, $W/W_0 = 0.595$ (a); $f_g = 0.15$, $W/W_0 = 0.621$ (b).

performed considering $L = 100\,mm$, out-of-plane thickness $L/10$, $E = 1MPa$, $\nu = 0.3$, $P = 1N$. In Table 1, values of the maximum deflection read under the loaded points are reported for the achieved optimal distribution of material (multi-scale design), as well as for full-scale finite element analyses of the blueprints. The maximum deflection occurs at the node where the central load P_2 is applied. When computed for the truss blueprint, it is 5% larger than that read for the blueprint of the sandwich specimen. According to a two-dimensional linear buckling analysis, the first eigenvalue computed for the latter is almost three times that found when analyzing the former.

As expected, the sandwich structure outperforms the truss design in terms of in-plane stability of the component, due to the remarkably higher bending stiffness-to-weight ratio, see in particular [58]. Notwithstanding the relatively big value of d, the computed deflections seem in line with the predictions of the multi-scale model used in the optimization.

A final investigation is performed controlling not only the displacements involved in the definition of the work of the external forces, as done above, but also the horizonal displacement at the roller. The former constraints are responsible for the arising of a final layout that is able to carry the loads with limited deflection of the beam, whereas the latter may be seen as an additional serviceability condition (referring in this case to the adopted bearing device). In the simula-

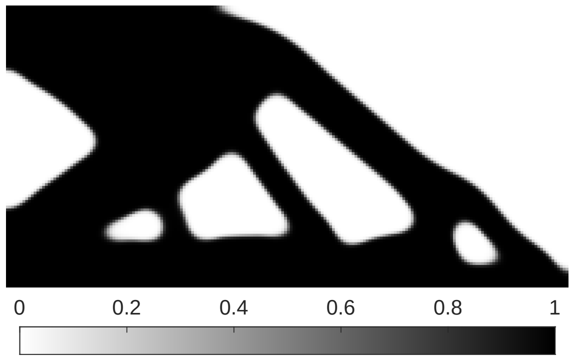

Figure 14: Example 2. Optimal design for $f_g = 0$, $W/W_0 = 0.556$.

tions presented next, the horizontal displacement at the roller is required not to exceed the value computed for the entire domain made of full material. Four additional constraints are needed to control the displacement, considering the multiple load cases. In Figure 13(a), the optimal solution achieved for $f_g = 0$ is presented. Compared to that presented in Figure 9, a more branched layout arises to meet the prescribed enforcement on the horizontal displacement, at the cost of a 10% increase in terms of weight. In Figure 13(b) the optimal solution found for $f_g = 0.15$ is reported, consisting of a sandwiched region integrated with elements made of full material. Compared to the layout achieved for the same amount of graded material in Figure 10(c), the additional control of the horizonal displacement at the roller calls for a 8% increase in the final weight.

4.2. Design of a cantilever beam under a uniformly distributed load

The optimal design of the $2L \times L$ cantilever beam in Figure 7(b) is dealt with, adopting a mesh of 200×100 square finite elements. A uniformly distributed load with intensity q acting along the entire lower edge of the rectangular design domain is considered in the optimization. The vertical displacement of each one of the nodes along the edge is controlled by means of a local constraint. In this example, the modified augmented lagrangian approach detailed in Section 3.2.2 handles

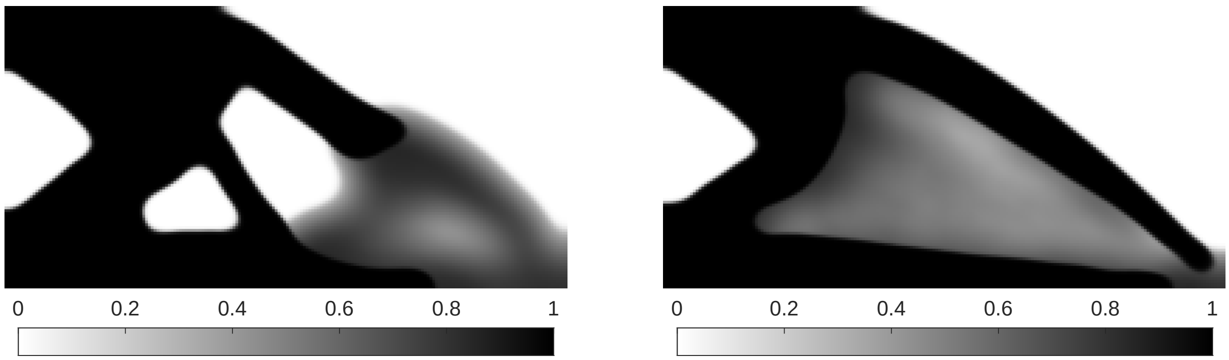

(a) (b)

Figure 15: Example 2. Optimal design for: $f_g = 0.125$, $W/W_0 = 0.576$ (a); $f_g = 0.15$, $W/W_0 = 0.578$ (b).

200 enforcements of the type in Eqn. (11c), along with the constraint governing the minimum amount of graded material to be distributed, namely Eqn. (11d).

At first, the case $f_g = 0$ is considered. The map of element densities $\rho_e+(1-\rho_e)\rho_{g,e}$ achieved by the implemented multi-constrained formulation is given in Figure 14. A black-and-white solution is found, namely $\rho_{g,e} = 0$ in the entire design domain. A thick horizontal element, which collects the orthogonal load while acting as a strut, is hanging from the upper part of the truss through a system of multiple ties. The weight ratio at convergence is $W/W_0 = 0.556$.

A minimum amount of graded material appears in the optimal solution, if $f_g > 0$ is enforced in the solution of Eqn. (11). In Figure 15(a) and Figure 15(b) the optimal solutions achieved by setting $f_g = 0.125$ and $f_g = 0.15$ are shown, respectively. In the former case, the tip of the cantilever beam, i.e. its less stressed part, is made of porous material. The graded area is supported, from below, by a tapered horizontal element made of full material and, from above, by a single tie. Indeed, the remaining part resembles a standard truss. The final weight ratio is $W/W_0 = 0.576$. In the latter case, the optimal design is not far from the type of solution already seen in Figure 10(d). Indeed, only the very last end of the tip of the arising cantilever beam is

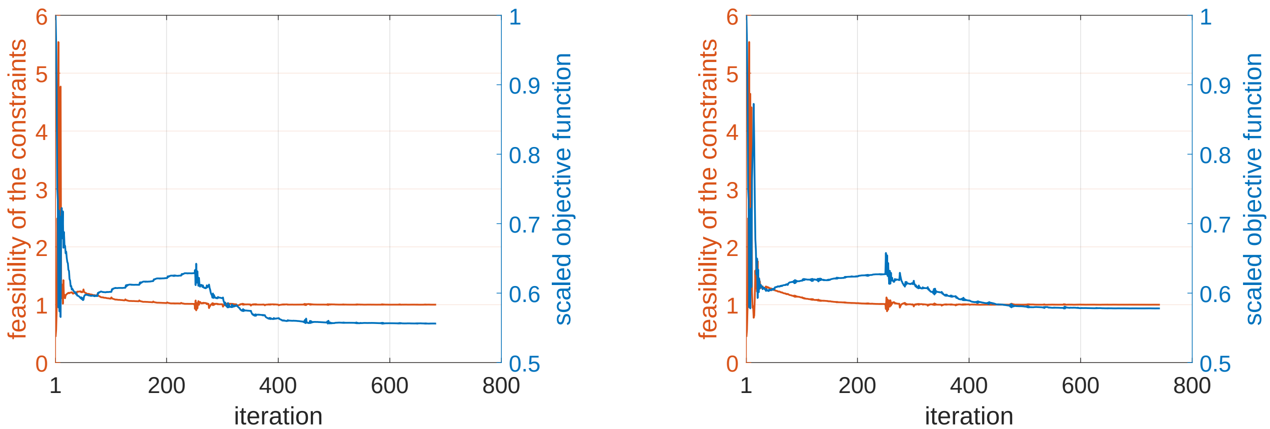

(a) (b)

Figure 16: Example 2. History plot of the scaled objective function W/W_0 and of the feasibility of the constraints: $f_g = 0$, final $W/W_0 = 0.556$ (a); $f_g = 0.15$, final $W/W_0 = 0.578$ (b).

made of graded material only, whereas most of the porous phase is surrounded by a thick coating of solid material. The final weight ratio for the latter design is $W/W_0 = 0.578$, only 4% more than the truss design in Figure 14.

In Figure 16, the history plots of the scaled objective function W/W_0 and the feasibility of the constraints are presented for the minimization problems concerning the design in Figure 14, with $f_g = 0$, and the layout in Figure 15(d), with $f_g = 0.15$. The represented feasibility refers to the maximum value of the left hand side of Eqn. (11c) and Eqn. (11d) written as $u_i/u_{lim,i} \leq 1$ and $f_g \sum_{e=1}^{n} W_{0,e} / \sum_{e=1}^{n} (1-\rho_e)\rho_{g,e} W_{0,e} \leq 1$, respectively. The optimization is initialized with $\rho_e = 1$ and $\rho_{g,e} = 0$ everywhere. The continuation scheme for p is such that the initial value $p = 3$ is used for the first 50 iterations, whereas an increase of 0.25 is given every 25 iterations until $p = 6$, see Section 2.4. The parameter β, both for Eqn. (14) and Eqn. (15), is equal to 2 in the first 250 iterations; then it increases by 2 every 25 iterations until $\beta = 16$, see Section 3.2.1. As expected, the continuation approach used with p is responsible for an increase in the objective function, whereas that used with β is related to a decrease. Both simulations end with full feasibility of the

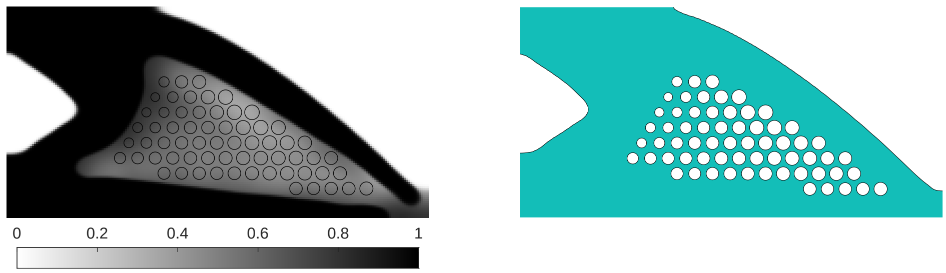

(a) (b)

Figure 17: Example 2. Design for $f_g = 0.15$, $d = L/12$: overlay of the HPC circular holes and of the optimal distribution of material density (a); final layout (b).

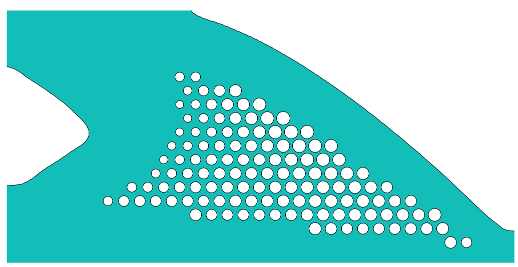

Figure 18: Example 2. Design for $f_g = 0.15$, $d = L/16$: final layout.

enforced constraints.

For the component with $f_g = 0.15$, two possible final layouts are given in Figure 17 and 18, for $d = L/12$ and $d = L/16$ respectively. In Figure 17(a) an overlay of the optimal distribution of material density and of the set of the graded circular holes is provided, as well.

Full-scale finite element analyses have been performed for a preliminary assessment of the structural behaviour of the blueprints represented in Figure 17(b) and Figure 18, with respect to the blueprint of the solid-and-void design shown in Figure 14. The final weight ratio for the truss-like layout is $W/W_0 = 0.569$. It increases to $W/W_0 = 0.608$ when processing the design for $f_g = 0.15$ using $d = L/12$. For the same density distribution, the adoption $d = L/16$ provides a better approximation of the grey area, and the relevant weight ratio reads $W/W_0 = 0.598$. Meshes of about $15 \cdot 10^3$ quadrangular elements have been generated by enforcing a maximum edge length equal to $7.5 \cdot 10^{-3}L$. Numerical simulations have been performed considering $L = 100\,mm$, out-of-plane thickness $L/10$, $E = 1MPa$, $\nu = 0.3$, $q = 0.01N/mm$. In Table 1, values of the maximum deflection read at the tip are reported for the achieved optimal distribution of material (multi-scale design), and for full-scale finite element analyses of the blueprints.

At first, the uniformly distributed load with intensity q is considered in the simulations. The maximum deflection read at the tip of the blueprint of the truss-like layout is 3% and 2% larger than that read for the full-scale models of the blueprints of Figure 17 and Figure 18, respectively. When homogenization is used within topology optimization, full-scale analyses are recommended to check that a suitable separation of scales (porous material/structure) exists, such that the multi-scale framework may be effectively relied upon [10]. To this extent, the very small variation that can be read in Table 1 looking at the values v^{max} computed via full-scale analyses of the blueprints with $d = L/12$ and $d = L/16$, confirms the validity of the multi-scale approach used in the optimization, at least from an engineering point of view.

A further numerical investigation is performed assuming a variation in the load distribution. Denoting by x the horizontal axis spanning from the left end of the lower edge of the rectangular design domain, the intensity $q_{var} = 5/32\,qx^4/L^4$ is accounted for to shift the (equal) resultant into the right half of the domain. The maximum deflection read at the tip of the blueprint of the truss-like layout is 15% larger than that found in case of uniformly distributed load. As expected, the blueprints originated from the multi-scale design for $f_g = 0.15$ exhibit increased robustness with respect to force variations. For both, the decrease in terms of overall stiffness is around 7%, less than one half that reported for $f_g = 0$.

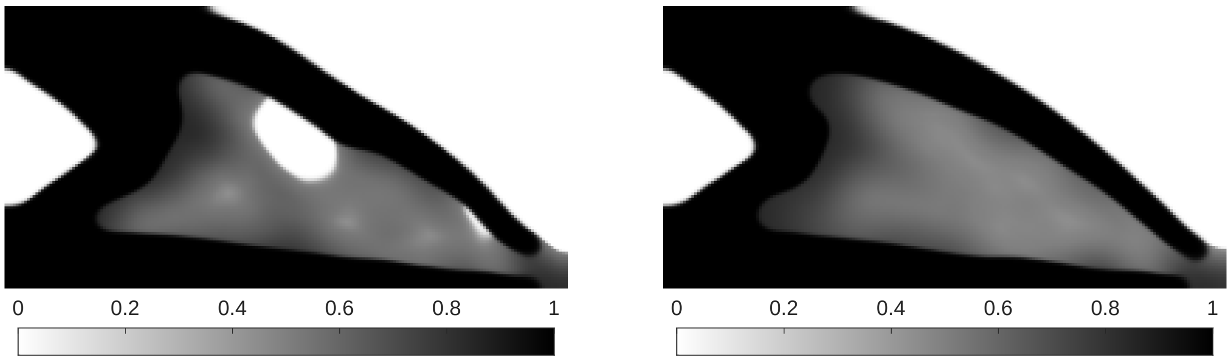

(a) (b)

Figure 19: Example 2. Optimal design with $\rho_{g,min} = 0.45$ for: $f_g = 0.15$, $W/W_0 = 0.579$ (a); $f_g = 0.175$, $W/W_0 = 0.582$ (b).

The adoption of the two-material law presented in Section 2.4 allows controlling the minimum value of the porous material density, $\rho_{g,min}$, in conjunction with a projection of the filtered variables $\rho_{g,e}$, see Section 3.2.1. To assess this feature, the optimization is re-run enforcing $\rho_{g,min} = 0.45$, instead of the value adopted previously ($\rho_{g,min} = 0.30$). The design found for $f_g = 0.15$ is reported in Figure 19(a). The layout of the solid material is not far from that found for the same value of f_g but smaller $\rho_{g,min}$, see Figure 15(b). However, two void areas break the continuity of the graded material inside the solid elements. The final weight ratio for the latter design is $W/W_0 = 0.579$, approximately the same as the previous result. By allowing for a larger amount of porous material, i.e. using $f_g = 0.175$, the continuity of the inner graded region is recovered, with a weight ratio $W/W_0 = 0.582$, see Figure 19(b). In this case, the increase in $\rho_{g,min}$ can be compensated for by the enforcement of a larger f_g: the type of optimal solution is not affected, whereas the layout of the components (porous and solid material) is re-arranged with a minor increase in weight.

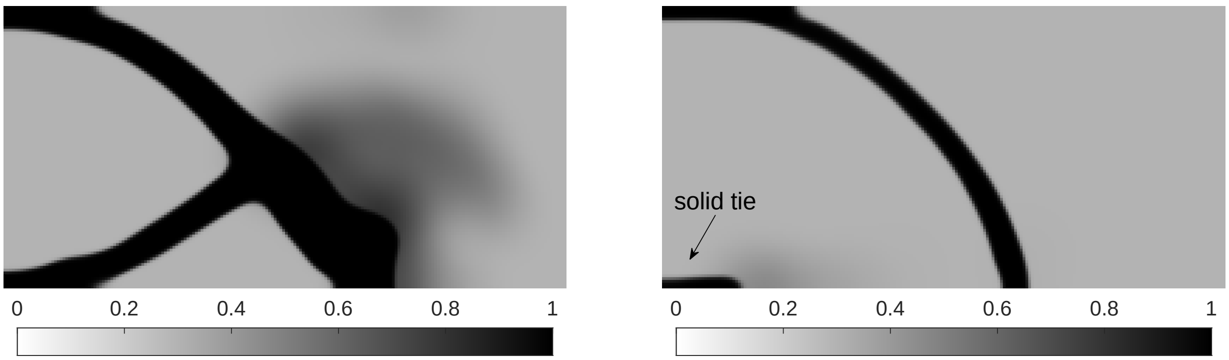

(a) (b)

Figure 20: Example 3. Optimal design considering: distributed load only, $W/W_0 = 0.491$ (a); self-weight only, $W/W_0 = 0.354$ (b).

4.3. Optimal grading for an infill problem

An infill problem is dealt with, addressing a $4L \times L$ simply-supported beam. The rectangular shape of the boundary is fixed, and the infill of minimum weight is sought considering the structural response to two types of load: (i) a uniformly distributed one acting along the upper edge and (ii) self-weight. Due to symmetry in load and geometry, only the right half of the beam is discretized, as shown in Figure 7(c). A mesh of 200×100 square finite elements is adopted to perform the numerical study.

The formulation in Eqn. (11) is implemented, controlling the vertical displacement of each one of the unrestrained nodes located along the lower edge of the specimen. As detailed in Section 3, when dealing with infill problems, $\rho_{g,min}$ and $\rho_{g,max}$ are enforced through side constraints. The adoption of the two-phase material law of Section 2.4 prevents the arising of porous material in the range $\rho_{g,max}$-1. Void is not allowed, because $\rho = \rho_g = 0$ is not a feasible solution for the problem. No control is operated on the minimum amount of graded material, i.e. $f_g = 0$ is set in Eqn. (11d).

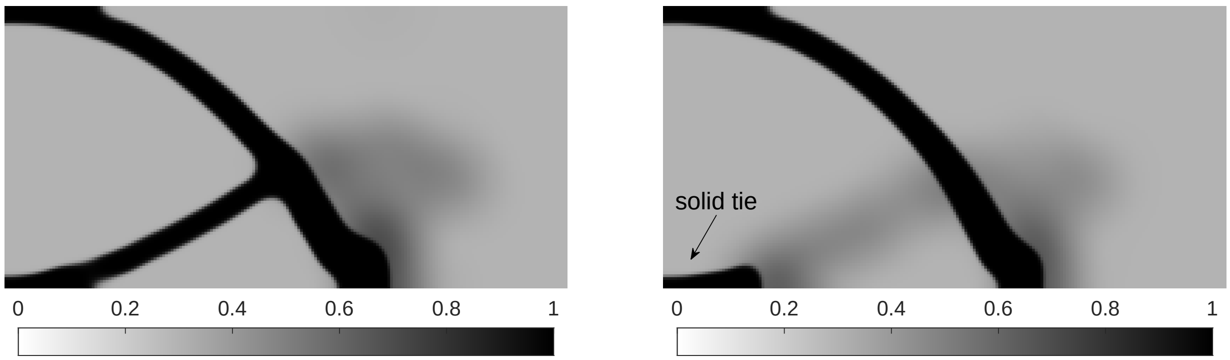

(a) (b)

Figure 21: Example 3. Optimal design considering: distributed load and self-weight, $W/W_0 = 0.425$ (a); half distributed load and self-weight, $W/W_0 = 0.404$ (b).

At first, the optimization is performed considering only the distributed load. The map of element densities $\rho_e + (1 - \rho_e)\rho_{g,e}$ achieved by the implemented multi-constrained formulation is given in Figure 20(a). The weight ratio at convergence reads $W/W_0 = 0.491$. This means that the weight of the filled specimen is nearly one half of the specimen made of full material (whereas the deflection of the former is one and half that of the latter). In the inner part of the specimen a sort of lenticular truss arises. Two chords made of full material surround an inner area of porous phase, whose density is nearly homogenous and equal to $\rho_{g,min}$. In the lateral overhang, load transferring is provided by the graded porous phase only. The highest density of the porous material is found within a region centered on the beam support.

Then the optimization is performed considering only the self-weight, which is implemented as a consistent load in the finite element model. The final result is presented in Figure 20(b). The solid phase consists of an arch-like structure spanning between the supports. The horizontal thrust is sustained by a solid tie, which spreads in porous material when moving towards the restraints. Porous material of lower density arises elsewhere. The weight ratio of the this optimal layout reads

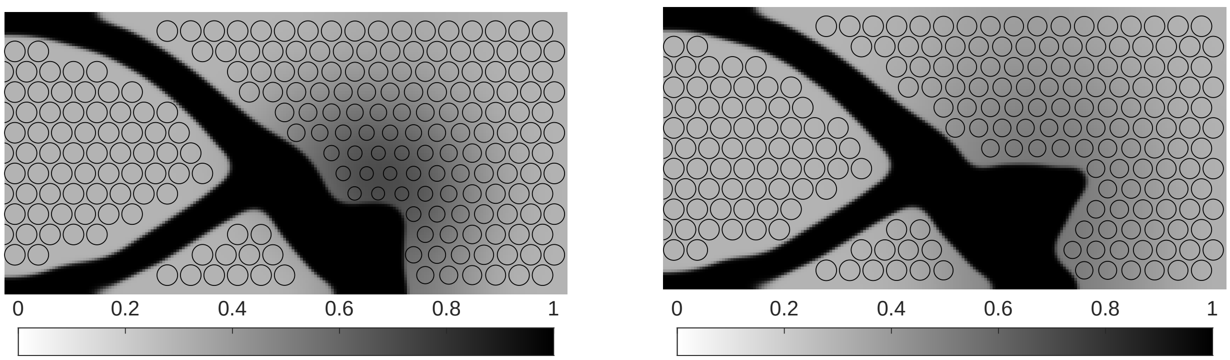

(a) (b)

Figure 22: Example 3. Overlay of the HPC circular holes ($d = L/12$) and of the optimal distribution of material density considering distributed load only: for $r_{g,f} = 4r_f$, $W/W_0 = 0.495$ (a); for $r_{g,f} = 6r_f$, $W/W_0 = 0.500$ (b).

$W/W_0 = 0.354$. This means that, reducing by approximately two third the weight of the specimen made of full material, the maximum deflection increases by half. Indeed, removing material implies not only a loss in stiffness, but also a decrease in load, see the non-monotonous sensitivity in Eqn. (B.4). This was originally discussed in [67], addressing design-dependent minimum compliance problems of topology optimization.

In Figure 21, optimal results found for loads i) and ii) that act simultaneously are shown. At first, it is assumed that the resultant of the distributed load equals the weight of the entire specimen made of full material. The achieved design, see Figure 21(a), is similar to that found when considering only the distributed load. However, the chords of the lenticular truss are thinner and the porous material around the support is less dense. This implies a lower weight ratio, namely $W/W_0 = 0.425$. Then, self-weight is coupled with a distributed load with half the intensity considered above. In this case, the design is dominated by the design-dependent load. A heavier version of the solution shown in Figure 20(b) is represented in Figure 21(b). In this case, a region of graded material with $\rho_{g,e} > \rho_{g,min}$ connects the tie to the outer arch, while strengthening the

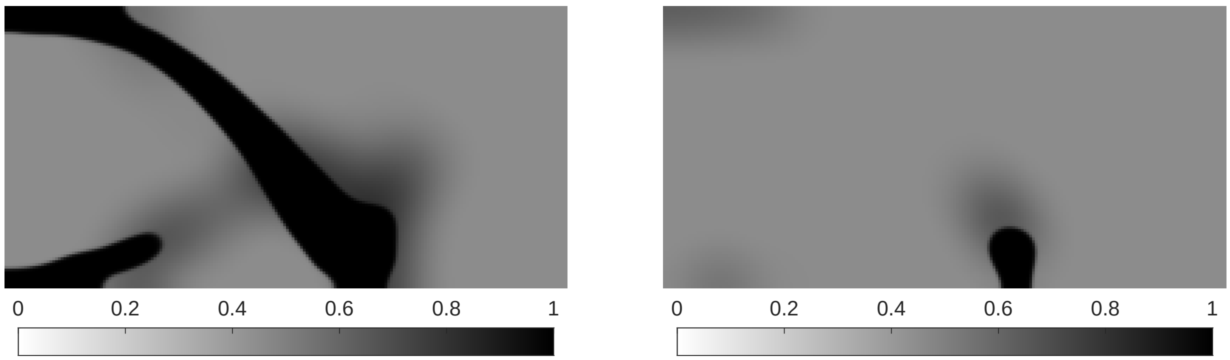

(a) (b)

Figure 23: Example 2. Optimal design with $\rho_{g,min} = 0.45$ considering: distributed load only, $W/W_0 = 0.574$ (a); self-weight only, $W/W_0 = 0.469$ (b).

overhang next to the support. The weight ratio at convergence, namely $W/W_0 = 0.404$, is lower than that of the design in Figure 21(a).

The optimization of the infill considering only the distributed load is revisited by investigating the effect of an increase in the filter radius adopted to manipulate the porous phase $r_{g,f}$. In Figure 22(a) and 22(b) the optimal distribution of material density is given as found using $r_{g,f} = 4r_f$ and $r_{g,f} = 6r_f$, respectively. In the same pictures, the set of the graded circular holes that may be computed for $d = L/12$ according to the post-processing procedure detailed in Section 3.3 is given, as well. As expected, an increase in $r_{g,f}$ promotes a smoother variation in the spatial distribution of $\rho_{g,e}$. This has a minor effect on the final weight, whereas some impact is reported also on the distribution of the solid phase. Reference is made to the layout in the vicinity of the support in Figure 22(a) and in Figure 22 (b), compared to that shown in Figure 20(a).

A further test is performed considering the optimal infill problem while enforcing $\rho_{g,min} = 0.45$, instead of the value adopted in the previous simulations ($\rho_{g,min} = 0.30$). This is operated as a modification of the side constraints of the variables $\rho_{g,e}$. The case of distributed load only, and

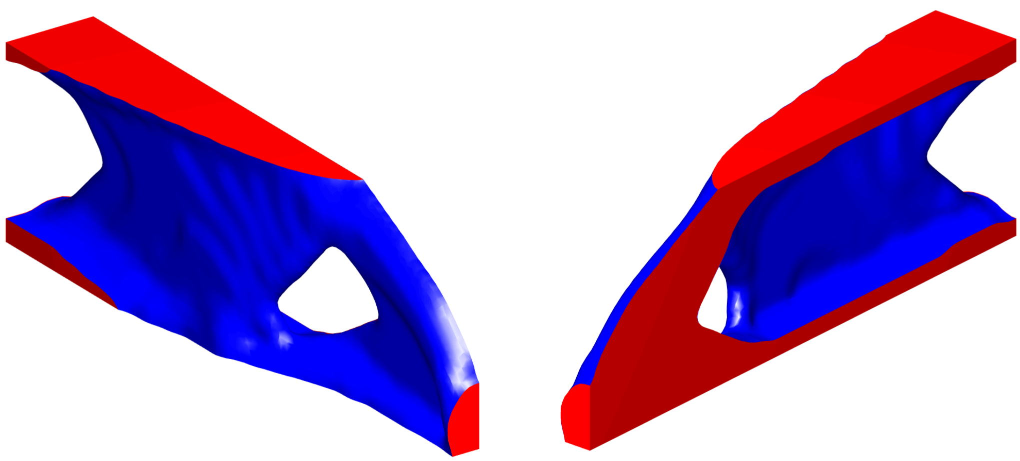

(a) (b)

Figure 24: Example 4. Final design for $f_g = 0$, $W/W_0 = 0.242$: external view (a); internal view (b).

self-weight only are considered, see results in Figure 23. The infill problem is particularly sensitive to $\rho_{g,min}$. By comparing the achieved solutions with those already found for the reference value, see Figure 20, noticeable changes in terms of both design and weight ratio may be pointed out. When the distributed load is applied, part of the solid lenticular truss is replaced by porous material and the overall increase in weight is around 15%. Considering the self-weight only, the solid structure disappears in favour of graded material, except for a small region around the support. With respect to the reference solution, this costs an increase in terms of weight around 25%.

4.4. Design of a three-dimensional cantilever beam

A three-dimensional application is considered.The $3L \times L \times L$ cantilever beam shown in Figure 8 is herein analyzed considering three load cases: i) P_1, ii) P_2, iii) P_1, P_2 acting simultaneously. Vertical forces are such that the resultant of P_1 is equal to that of P_2. Due to symmetry in geometry and load, only one half of the specimen is analyzed, using a mesh of $108 \times 36 \times 18$ cubic elements.

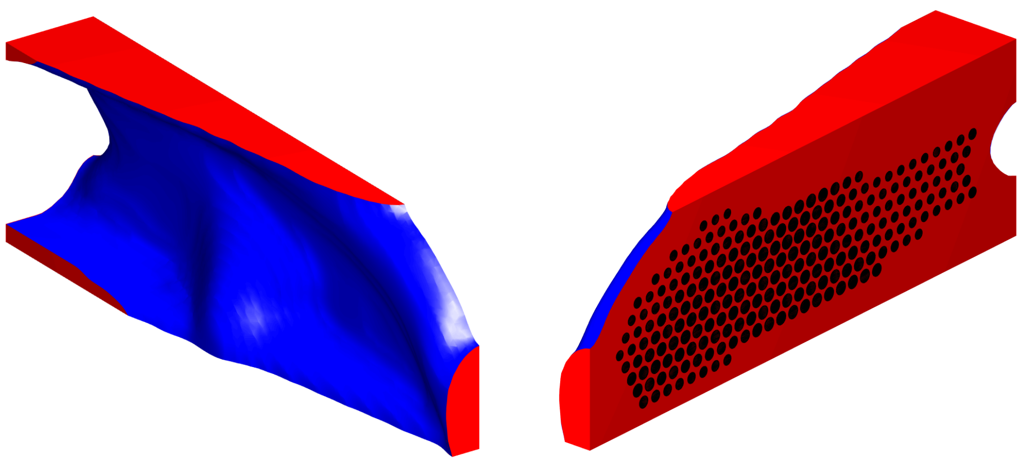

(a) (b)

Figure 25: Example 4. Final design for: $f_g = 0.10$, $W/W_0 = 0.274$, $d = L/12$: external view (a); internal view (b).

The deflection control is operated at the loaded nodes: 6 nodes are used to address P_1 and the same for P_2.

The implementation in the three-dimensional framework is fully along the lines of the two-dimensional algorithm. In this extension, the element matrices $\mathbf{K}_{K0,e}$ and $\mathbf{K}_{G0,e}$ of Section 3.1 are computed using brick shape functions and three-dimensional elasticity. The two-phase material law of Section 2.4 allows for the distribution of full material and void, along with a fraction of porous microstructure with graded spherical holes. Indeed, $K(\rho_g)$ and $G(\rho_g)$ are those derived in Section 2.3. It must be remarked that the proposed algorithm, which exploits regular meshes and employs the gradient-based Methods of Moving Asymptotes [30], is well-suited to be implemented within large-scale fully parallelized optimization framework, as the one implemented in [68], to allow for an accurate description of the geometry of the optimal layouts.

The solution found for $f_g = 0$ is presented in Figure 24. An external and an internal view of the considered half part of the specimen are shown. Following [43], an iso-surface of the smoothed element densities $\rho_e + (1 - \rho_e)\rho_{g,e}$ is employed to represent the boundaries of the optimized object. No fraction of graded material arises. The optimal design consists of a box-shaped structure connected with a truss-like tip, both made of full material only. Reference is made to [69] for a discussion about optimality of closed-walled layouts for pure stiffness optimization. The weight ratio of the achieved layout reads $W/W_0 = 0.242$.

The optimal solution found for $f_g = 0.10$ is presented in Figure 25. As before, the boundaries of the optimized object are sketched by means of an iso-surface of the smoothed element densities. The post-processing procedure in Section 3.3 is used with $d = L/12$ to compute position and radius of the spherical holes corresponding to the achieved distribution of the quantity $(1 - \rho_e)\rho_{g,e}$. The comments already formulated for the two-dimensional examples on the selection of d, apply here as well. The optimal layout has a final weight ratio of $W/W_0 = 0.274$, approximately 13% more than the previous one. The external shape of the object is not far from that represented in Figure 24. However, the internal cavity is replaced by graded porous microstructures, with some benefit, among the others, for layer-by-layer manufacturing.

The history plots of the scaled objective function W/W_0 and of the feasibility of the constraints for the considered three-dimensional problems are reported in Figure 26. Similar features to those already outlined for the curves in Figure 16 can be pointed out.

5. Conclusions

While most of the available methods for multi-scale topology optimization deal with compliance minimization, a multi-scale approach of topology optimization has been proposed in this contribution to design structural components of minimum weight for given loads and displacement limits. Numerical homogenization has been implemented to derive the macroscopic elastic properties of hexagonal close-packed (HCP) arrangements of circular and spherical holes, depending on the radius of their cavities. An isotropic and a transversely isotropic constitutive laws ap-

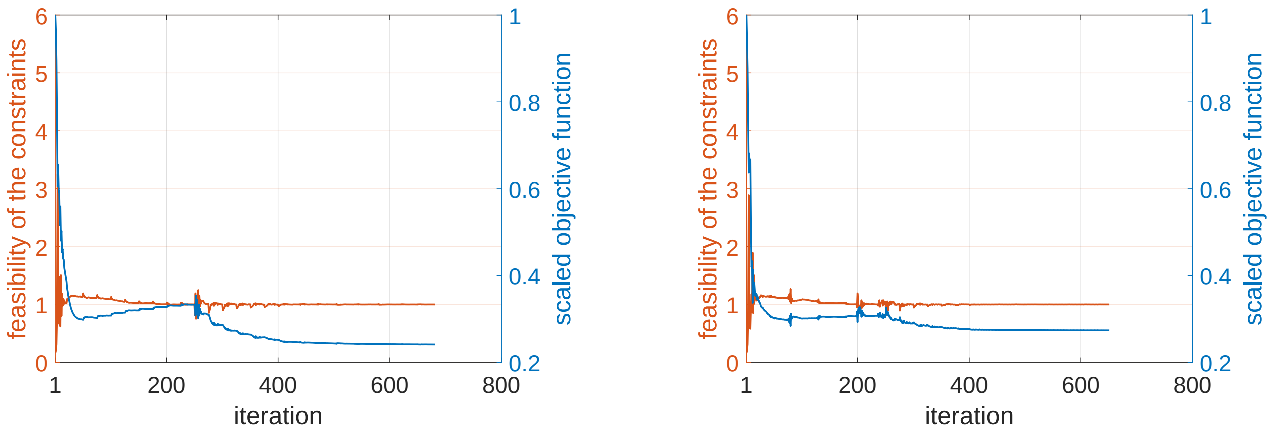

(a) (b)

Figure 26: Example 2. History plot of the scaled objective function W/W_0 and of the feasibility of the constraints: $f_g = 0$, final $W/W_0 = 0.242$ (a); $f_g = 0.10$, final $W/W_0 = 0.274$ (b).

ply in the two-dimensional and the three-dimensional cases, respectively. Due to the moderate anisotropy that has been found to affect the three-dimensional microstructure, the macroscopic elastic properties of both porous phases have been derived in terms of the bulk modulus and the shear modulus, with varying density. A multi-material interpolation law has been adopted to distribute, simultaneously, a solid phase of the material, a graded porous phase, and void. Filtering and projection procedures have been used in conjunction with the adopted material law to promote smooth density distributions, avoiding the arising of porous material out of a given density range. Indeed, minor modifications are needed with respect to the implementation of a conventional SIMP-based topology optimization approach, which penalizes the Young's modulus only. Multiple displacement constraints arise when dealing with several control points and/or load cases, as requested e.g. in the design of structural components at the serviceability limit state. Besides the control of the maximum and minimum density of the graded material to be distributed along with the solid and void phase, the proposed material law has been especially conceived to control the amount of porous phase. Indeed, an enforcement governing the minimum amount of graded porous microstructure to be used in the optimal design has been considered, as well. Following recent outcomes of stress-constrained optimal design, an Augmented Lagrangian method has been implemented to handle the arising multi-constrained problem, thus providing a preliminary assessment of the adopted AL method in conjunction with multiple displacement constraints and the multi-material interpolation law. Numerical simulations have mainly explored the control of displacements involved in the definition of the work of the external forces. The control of a displacement component not related to the compliance has been tested too. The result of the topology optimization procedure is an optimal distribution of overall material density, which allows for a straightforward detection of the region made by the solid and the graded phase. A simple post-processing technique has been discussed to define i) boundaries of the component, and, ii) possible internal arrangements of circular/spherical holes with graded radius. Alternatively, when boundaries of a hollow component are given, the approach provides the geometry of an optimal infill. Indeed, the shape of two-dimensional and three-dimensional blueprints can be straightforwardly exported for manufacturing, in particular AM, considering the graphical information both at the macro- and at the micro- scale. It is remarked that the prescribed value of the minimum density of the graded material may remarkably affect the layout in problems of optimal infill, especially when considering the self-weight.

As expected, when disregarding the constraint on the amount of graded porous microstructure, minimum weight layouts that consist only of full material (and void) have been found: trusses, for the two-dimensional applications, and a component embedding a box-shaped structure, for the three-dimensional numerical example. By prescribing a small amount of porous phase in the optimal design, solutions to the displacement-constrained optimization problem have been attained at the cost of a minor increase in terms of weight. Among the achieved layouts, coated structures, i.e. components made of a solid coating that encloses a region of porous material, have been retrieved for different types of loads and displacement constraints. A peculiar feature of the proposed approach is that both the thickness and the location of the coating, if any, are an outcome of the optimization procedure. It must be remarked that conventional homogenization methods are based on the assumption of separation of scale, meaning that the microstructure should consist of relatively small heterogeneities, to give an adequate estimate of the average macroscopic properties. Full-scale finite elements analyses have been performed on two-dimensional blueprints, also considering different reference sizes for the porous microstructure, showing good agreement between the computed displacements and those predicted within the framework of the implemented multi-scale approach. These FE models have been used to assess well-known beneficial features provided by porous structures, such as high bending stiffness-to-weight ratio to increase buckling loads and robustness with respect to force variations. A preliminary test has been performed to investigate printability of the circular/spherical holes by means of layer-by-layer additive manufacturing processes. Indeed, the arising of layouts that employ areas of graded material instead of void regions may alleviate issues related to the support of extended cavities.

The ongoing research is mainly devoted to the extension of the proposed procedure to large-scale problems, endowing the formulation with other kind of local constraints, such as failure constraints, see in particular [52] and [70]. Further development includes accounting for the effect of load uncertainties in the derivation of the optimal multi-scale design, see [71].

Acknowledgement

The first three authors wish to thank the National Research, Development and Innovation Office of Hungary (grant K 138615).

Data availability statement

No unreferenced data are required to reproduce the findings presented above. To facilitate replication of the results, the manuscript discusses the formulation in detail and provides the input parameters used to run the numerical examples.

Appendix A.

For a transversally isotropic material having y_3 as the axis of symmetry, the components of the stress tensor may be written in term of those of the strain tensor as:

$$\begin{bmatrix} \sigma_{11} \\ \sigma_{22} \\ \sigma_{33} \\ \sigma_{13} \\ \sigma_{23} \\ \sigma_{12} \end{bmatrix} = \begin{bmatrix} C_{11} & C_{12} & C_{13} & 0 & 0 & 0 \\ & C_{11} & C_{13} & 0 & 0 & 0 \\ & & C_{33} & 0 & 0 & 0 \\ & & & C_{44} & 0 & 0 \\ & \text{syms} & & 0 & C_{44} & 0 \\ & & & 0 & 0 & \frac{1}{2}(C_{11}-C_{12}) \end{bmatrix} \begin{bmatrix} \varepsilon_{11} \\ \varepsilon_{22} \\ \varepsilon_{33} \\ 2\varepsilon_{13} \\ 2\varepsilon_{23} \\ 2\varepsilon_{12} \end{bmatrix}, \tag{A.1}$$

where C_{11}, C_{12}, C_{13}, C_{33}, C_{44} are five independents elastic constants. For the graded porous microstructure described in Section 2.3, a deviation from the isotropic behavior can be appreciated only for low material densities. Figure A.27 shows dependence of the Young modulus on the direction, for two different values of the density. Colour, as well as distance of the surface points from the center, represents E/E_0 along the corresponding direction. For $\rho_g = 0.62$ (a) a sphere is found, whereas some minor deviation arises for $\rho_g = 0.33$, due to an increased stiffness at the poles along the y_3-axis (b). The above results suggest the adoption of the isotropic material model as a reasonable approximation to handle the three-dimensional porous microstructure in the multi-scale approach of topology optimization. To avoid overestimating the elastic constants, the shear modulus G is computed from C_{44}, whereas the bulk modulus K from C_{11}, i.e. assuming that $G(\rho_g) = C_{44}(\rho_g)$ and $K(\rho_g) = C_{11}(\rho_g) - 4G(\rho_g)/3$.

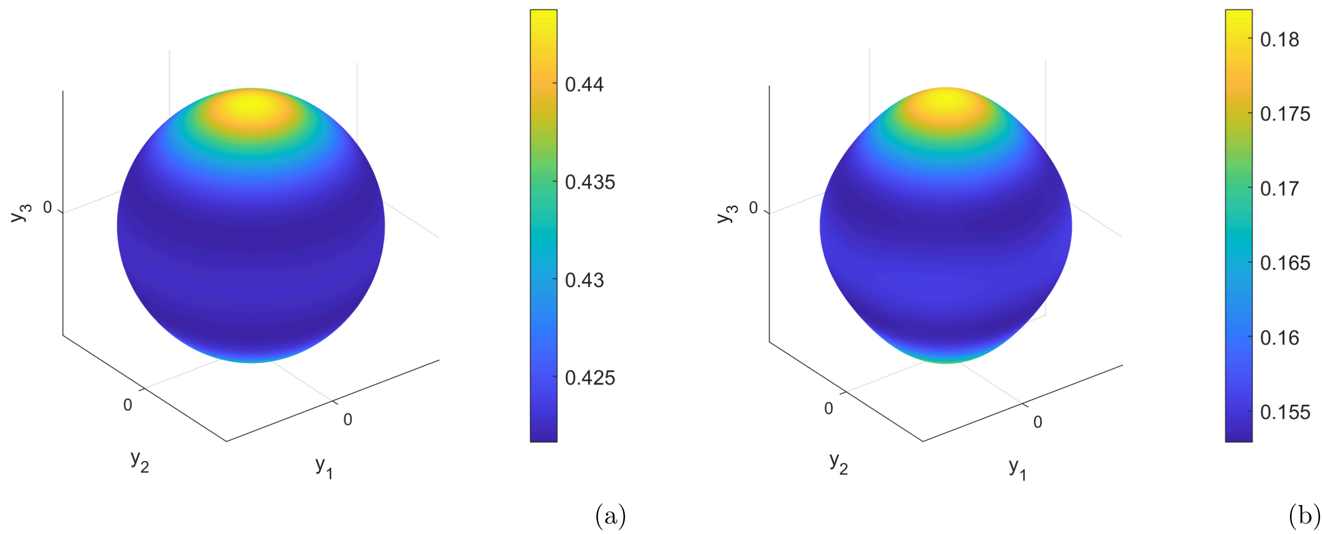

Figure A.27: 3D version of the porous microstructure: dependence of the Young modulus on the direction (colour, as well as distance of the surface points from the center, represents E/E_0 in the corresponding direction): $\rho_g = 0.62$ (a); $\rho_g = 0.33$ (b).

670 ## Appendix B.

The sensitivity of the objective function and of the constraints in Eqn. (11) are computed through the adjoint method, see e.g. [2]. Accordingly, u_i in Eqn. (11c) does not change when adding at the right hand side a zero function derived from the equilibrium of Eqn. (11b):

$$-\boldsymbol{\lambda}_i^T \left(\mathbf{K}(\boldsymbol{\rho}, \boldsymbol{\rho_g})\mathbf{U}_j - \mathbf{F}_j(\boldsymbol{\rho}, \boldsymbol{\rho_g})\right), \tag{B.1}$$

where $\boldsymbol{\lambda}_i$ is any arbitrary but fixed vector and $\mathbf{F}_j = \mathbf{F}_j(\boldsymbol{\rho}, \boldsymbol{\rho_g})$, i.e. the case of design-dependent loads such as self-weight, is considered. The derivative of u_i with respect to the element unknown

ρ_s, which can be indifferently an entry either of $\boldsymbol{\rho}$ or of $\boldsymbol{\rho_g}$, may be computed as:

$$\frac{\partial u_i}{\partial \rho_s} = \boldsymbol{L}_i^T \frac{\partial \mathbf{U}_j}{\partial \rho_s} - \boldsymbol{\lambda}_i^T \frac{\partial \mathbf{K}(\boldsymbol{\rho}, \boldsymbol{\rho_g})}{\partial \rho_s} \mathbf{U}_j - \boldsymbol{\lambda}_i^T \mathbf{K}(\boldsymbol{\rho}, \boldsymbol{\rho_g}) \frac{\partial \mathbf{U}_j}{\partial \rho_s} + \boldsymbol{\lambda}_i^T \frac{\partial \mathbf{F}_j(\boldsymbol{\rho}, \boldsymbol{\rho_g})}{\partial \rho_s}. \tag{B.2}$$

After re-arrangement of terms, one has:

$$\frac{\partial u_i}{\partial \rho_s} = \left(\boldsymbol{L}_i^T - \boldsymbol{\lambda}_i^T \mathbf{K}(\boldsymbol{\rho}, \boldsymbol{\rho_g})\right) \frac{\partial \mathbf{U}_j}{\partial \rho_s} - \boldsymbol{\lambda}_i^T \frac{\partial \mathbf{K}(\boldsymbol{\rho}, \boldsymbol{\rho_g})}{\partial \rho_s} \mathbf{U}_j + \boldsymbol{\lambda}_i^T \frac{\partial \mathbf{F}_j(\boldsymbol{\rho}, \boldsymbol{\rho_g})}{\partial \rho_s}, \tag{B.3}$$

that can be in turn written as:

$$\frac{\partial u_i}{\partial \rho_s} = -\boldsymbol{\lambda}_i^T \frac{\partial \mathbf{K}(\boldsymbol{\rho}, \boldsymbol{\rho_g})}{\partial \rho_s} \mathbf{U}_j + \boldsymbol{\lambda}_i^T \frac{\partial \mathbf{F}_j(\boldsymbol{\rho}, \boldsymbol{\rho_g})}{\partial \rho_s}, \tag{B.4}$$

where $\boldsymbol{\lambda}_i$ satisfies the adjoint equation:

$$\mathbf{K}(\boldsymbol{\rho}, \boldsymbol{\rho_g}) \boldsymbol{\lambda}_i = \left(\frac{\partial u_i}{\partial \mathbf{U}_j}\right)^T = \mathbf{L}_i. \tag{B.5}$$

The derivatives in Eqn. (B.4) can be evaluated accounting for the material law in Eqn. (10). The sensitivity of the objective function and the weight constraint in Eqn. (11c) are straightforward. The derivatives with respect to the filtered variables ($\tilde{\rho}_e$, $\tilde{\rho}_{g,e}$) and the projected ones ($\widehat{\rho}_e$, $\widehat{\rho}_{g,e}$) can be easily evaluated by applying the chain rule to Eqn. (13) and Eqns. (14-15), respectively. It is also remarked that, at each iteration, only one inverse of the stiffness matrix $\mathbf{K}(\boldsymbol{\rho}, \boldsymbol{\rho_g})$ must be computed to evaluate constraints and their sensitivities. Indeed the linear systems in Eqn. (11b) and Eqn. (B.5) share the same coefficient matrix.

References

[1] Bendsøe MP, Kikuchi N. Generating optimal topologies in structural design using a homogenization method. Comput Methods Appl Mech Eng 1988;71(2):197-224.

[2] Bendsøe MP, Sigmund O. Topology Optimization: Theory, Methods and Applications. Berlin: Springer; 2003.

[3] Bendsøe MP, Sigmund O. Material interpolation schemes in topology optimization. Arch Appl Mech 1999;69(9-10):635-654.

[4] Liu J, Gaynor AT, Chen S, Kang Z, Suresh K, Takezawa A, et al. Current and future trends in topology optimization for additive manufacturing. Struct Multidiscip Opt 2018;57(6):2457-2483.

[5] Plocher J, Panesar A. Review on design and structural optimisation in additive manufacturing: Towards next-generation lightweight structures. Mater Des 2019;183.

[6] Meng L, Zhang W, Quan D, Shi G, Tang L, Hou Y, et al. From Topology Optimization Design to Additive Manufacturing: Today's Success and Tomorrow's Roadmap. Arch Comput Methods Eng 2020;27(3):805-830.

[7] Fu J, Li H, Gao L, Xiao M. Design of shell-infill structures by a multiscale level set topology optimization method. Comput Struct 2019;212:162-172.

[8] Allaire G, Dapogny C, Estevez R, Faure A, Michailidis G. Structural optimization under overhang constraints imposed by additive manufacturing technologies. J Comput Phys 2017;351:295-328.

[9] Wang C, Zhang W, Zhou L, Gao T, Zhu J. Topology optimization of self-supporting structures for additive manufacturing with B-spline parameterization. Comput Methods Appl Mech Eng 2021;374.

[10] Wu J, Sigmund O, Groen JP. Topology optimization of multi-scale structures: a review. Struct Mutltidiscip Opt 2021;63(3):1455-1480.

[11] Guedes J, Kikuchi N. Preprocessing and postprocessing for materials based on the homogenization method with adaptive finite element methods. Comput Methods Appl Mech Eng 1990;83(2):143-198.

[12] Bensoussan A, Lions JL, Papanicolaou G. Asymptotic Analysis for Periodic Structures. New York: North-Holland; 1978.

[13] Sotiropoulos S, Kazakis G, Lagaros ND. Conceptual design of structural systems based on topology optimization and prefabricated components. Comput Struct 2020;226.

[14] Jansen M, Pierard O. A hybrid density/level set formulation for topology optimization of functionally graded lattice structures. Comput Struct 2020;231.

[15] Ypsilantis K-, Kazakis G, Lagaros ND. An efficient 3D homogenization-based topology optimization methodology. Comput Mech 2021;67(2):481-496.

[16] Allaire G, Geoffroy-Donders P, Pantz O. Topology optimization of modulated and oriented periodic microstructures by the homogenization method. Comput Math Appl 2019;78(7):2197-2229.

[17] Djourachkovitch T, Blal N, Hamila N, Gravouil A. Multiscale topology optimization of 3D structures: A micro-architectured materials database assisted strategy. Comput Struct 2021;255.

[18] Eschenauer HA, Olhoff N. Topology optimization of continuum structures: A review. Appl Mech Rev 2001;54(4):331-390.

[19] Lochner-Aldinger I, Schumacher A. Homogenization method: Distribution of material densities. Shell Structures for Architecture: Form Finding and Optimization; 2014. p. 211-223.

[20] Sivapuram R, Dunning PD, Kim HA. Simultaneous material and structural optimization by multiscale topology optimization. Struct Multidiscip Opt 2016;54(5):1267-1281.

[21] Hu J, Luo Y, Liu S. Two-scale concurrent topology optimization method of hierarchical structures with self-connected multiple lattice-material domains. Compos Struct 2021;272.

[22] Groen JP, Sigmund O. Homogenization-based topology optimization for high-resolution manufacturable microstructures. Int J Numer Methods Eng 2018;113(8):1148-1163.

[23] Xu L, Qian Z. Topology optimization and de-homogenization of graded lattice structures based on asymptotic homogenization. Compos Struct 2021;277.

[24] Wang Y, Xu H, Pasini D. Multiscale isogeometric topology optimization for lattice materials. Comput Methods Appl Mech Eng 2017;316:568-585.

[25] Panesar A, Abdi M, Hickman D, Ashcroft I. Strategies for functionally graded lattice structures derived using topology optimisation for Additive Manufacturing. Addit Manuf 2018;19:81-94.

[26] Achtziger W. Topology Optimization of Discrete Structures, in Topology Optimization in Structural Mechanics, Rozvany GIN Ed. Vienna: Springer; 1997.

[27] Conway J, Sloane NJA. Sphere Packings, Lattices and Groups. New York: Springer-Verlag; 1999.

[28] Giraldo-Londoño O, Paulino GH. PolyStress: a Matlab implementation for local stress-constrained topology optimization using the augmented Lagrangian method. Struct Multidiscip Opt 2021;63(4):2065-2097.

[29] da Silva GA, Aage N, Beck AT, Sigmund O. Three-dimensional manufacturing tolerant topology optimization with hundreds of millions of local stress constraints. Int J Numer Methods Eng 2021;122(2):548-578.

[30] Svanberg K. The method of moving asymptotes-a new method for structural optimization. Int J Numer Methods Eng 1987;24(2):359-373.

[31] Bertsekas DP. Nonlinear programming, 2nd edn. Nashua: Athena Scientific; 1999.

[32] Day AR, Snyder KA, Garboczi EJ, Thorpe MF. The elastic moduli of a sheet containing circular holes. J Mech Phys Solids 1992;40(5):1031-1051.

[33] Sigmund O. New class of extremal composites. J Mech Phys Solids 2000;48(2):397-428.

[34] Vigdergauz S. Two-dimensional grained composites of extreme rigidity. J Appl Mech Trans ASME 1994;61(2):390-394.

[35] Thomsen CR, Wang F, Sigmund O. Buckling strength topology optimization of 2D periodic materials based on linearized bifurcation analysis. Comput Methods Appl Mech Eng 2018;339:115-136.

[36] Coelho PG, Guedes JM, Cardoso JB. Topology optimization of cellular materials with periodic microstructure under stress constraints. Struct Mutltidiscip Opt 2019;59(2):633-645.

[37] Collet M, Noël L, Bruggi M, Duysinx P. Topology optimization for microstructural design under stress constraints. Struct Mutltidiscip Opt 2018;58(6):2677-2695.

[38] Andreassen E, Andreasen CS. How to determine composite material properties using numerical homogenization. Comput Mater Sci 2014;83:488-495.

[39] Heitkam S, Drenckhan W, Titscher T, Weaire D, Kreuter DC, Hajnal D, et al. Elastic properties of solid material with various arrangements of spherical voids. Eur J Mech A Solids 2016;59:252-264.

[40] Dong G, Tang Y, Zhao YF. A 149 Line Homogenization Code for Three-Dimensional Cellular Materials Written in MATLAB. J Eng Mater Technol Trans ASME 2019;141(1).

[41] Sigmund O, Torquato S. Design of materials with extreme thermal expansion using a three-phase topology optimization method. J Mech Phys Solids 1997;45(6):1037-1067.

[42] Stegmann J, Lund E. Discrete material optimization of general composite shell structures. Int J Numer Methods Eng 2005;62(14):2009-2027.

[43] Ferrari F, Sigmund O. A new generation 99 line Matlab code for compliance topology optimization and its extension to 3D. Struct Multidiscip Opt 2020;62(4):2211-2228.

[44] Bruggi M. Topology optimization with mixed finite elements on regular grids. Comput Methods Appl Mech Eng 2016;305:133-153.

[45] Borrvall T, Petersson J. Topology optimization using regularized intermediate density control. Comput Methods Appl Mech Eng 2001;190(37-38):4911-4928.

[46] Bourdin B. Filters in topology optimization. Int J Numer Methods Eng 2001;50(9):2143-2158.

[47] Wang F, Lazarov BS, Sigmund O. On projection methods, convergence and robust formulations in topology optimization. Struct Multidiscip Opt 2011;43(6):767-784.

[48] Guest JK, Prévost JH, Belytschko T. Achieving minimum length scale in topology optimization using nodal design variables and projection functions. Int J Numer Methods Eng 2004;61(2):238-254.

[49] Kawamoto A, Matsumori T, Yamasaki S, Nomura T, Kondoh T, Nishiwaki S. Heaviside projection based topology optimization by a PDE-filtered scalar function. Struct Multidiscip Opt 2011;44(1):19-24.

[50] Christensen PW, Klarbring A. An introduction to structural optimization. Solid Mech Appl. Berlin: Springer; 2008;153.

[51] Zhu B, Zhang X, Zhang H, Liang J, Zang H, Li H, et al. Design of compliant mechanisms using continuum topology optimization: A review. Mech Mach Theory 2020;143.

[52] Collet M, Bruggi M, Duysinx P. Topology optimization for minimum weight with compliance and simplified nominal stress constraints for fatigue resistance. Struct Multidiscip Opt 2017;55(3):839-855.

[53] Liu K, Tovar A. An efficient 3D topology optimization code written in Matlab. Struct Multidiscip Opt 2014;50(6):1175-1196.

[54] Jiu L, Zhang W, Meng L, Zhou Y, Chen L. A CAD-oriented structural topology optimization method. Comput Struct 2020;239.

[55] Choi S, Ryu J, Lee M, Cha J, Kim H, Song C, et al. Support-free hollowing with spheroids and efficient 3D printing utilizing circular printing motions based on Voronoi diagrams. Addit Manuf 2020;35.

[56] Ameen W, Al-Ahmari A, Mohammed MK, Mian SH. Manufacturability of overhanging holes using electron beam melting. Metals 2018;8(6).

[57] Hunter LW, Brackett D, Brierley N, Yang J, Attallah MM. Assessment of trapped powder removal and inspection strategies for powder bed fusion techniques. Int J Adv Manuf Technol 2020;106(9-10):4521-4532.

[58] Clausen A, Aage N, Sigmund O. Exploiting Additive Manufacturing Infill in Topology Optimization for Improved Buckling Load. Engineering 2016;2(2):250-257.

[59] Casalotti A, D'Annibale F, Rosi G. Multi-scale design of an architected composite structure with optimized graded properties. Compos Struct 2020;252.

[60] Clausen A, Aage N, Sigmund O. Topology optimization of coated structures and material interface problems. Comput Methods Appl Mech Eng 2015;290:524-541.

[61] Wadbro E, Niu B. Multiscale design for additive manufactured structures with solid coating and periodic infill pattern. Comput Methods Appl Mech Eng 2019;357.

[62] Niu B, Wadbro E. Multiscale design of coated structures with periodic uniform infill for vibration suppression. Comput Struct 2021;255.

[63] Yoon GH, Yi B. A new coating filter of coated structure for topology optimization. Struct Multidiscip Opt 2019;60(4):1527-1544.

[64] Yi B, Yoon GH, Peng X. A simple density filter for the topology optimization of coated structures. Eng Optim 2021;53(12):2088-2107.

[65] Lazarov BS, Wang F, Sigmund O. Length scale and manufacturability in density-based topology optimization. Arch Appl Mech 2016;86(1-2):189-218.

[66] Niu B, Wadbro E. On equal-width length-scale control in topology optimization. Struct Mutltidiscip Opt 2019;59(4):1321-1334.

[67] Bruyneel M, Duysinx P. Note on topology optimization of continuum structures including self-weight. Struct Multidiscip Opt 2005;29(4):245-256.

[68] Aage N, Andreassen E, Lazarov BS. Topology optimization using PETSc: An easy-to-use, fully parallel, open source topology optimization framework. Struct Multidiscip Opt 2015;51(3):565-572.

[69] Sigmund O, Aage N, Andreassen E. On the (non-)optimality of Michell structures. Struct Multidiscip Opt 2016;54(2):361-373.

[70] Cheng L, Bai J, To AC. Functionally graded lattice structure topology optimization for the design of additive manufactured components with stress constraints. Comput Methods Appl Mech Eng 2019;344:334-359.

[71] Balogh B, Bruggi M, Lógó J. Optimal design accounting for uncertainty in loading amplitudes: A numerical investigation. Mech Based Des Struct Mach 2018;46(5):552-566.